JGR Planets

RESEARCH ARTICLE

10.1029/2025JE009202

Antum Crater: A Window Into Ganymede's Icy Evolution

Federico Tosi[1], Federico Colaiuta[1,2], Valentina Galluzzi[1], Elena Martellato[3], Francesca Zambon[1], Katrin Stephan[4], Namitha R. Baby[5], Lorenzo Bruzzone[6], Pasquale Palumbo[1], and Giuseppe Piccioni[1]

[1]Istituto Nazionale di Astrofisica—Istituto di Astrofisica e Planetologia Spaziali (INAF-IAPS), Rome, Italy, [2]Sapienza Università di Roma, Rome, Italy, [3]Istituto Nazionale di Astrofisica—Osservatorio Astronomico di Padova (INAF-OAPd), Padua, Italy, [4]German Aerospace Center (DLR), Institute of Space Research, Berlin, Germany, [5]University of Freiburg, Institute of Earth and Environmental Sciences (Geology), Freiburg, Germany, [6]Università degli Studi di Trento—Dipartimento di Ingegneria e Scienza dell'Informazione, Trento, Italy

Abstract Located within the extensive dark terrain of Marius Regio, in the anti-Jovian trailing quadrant of Ganymede, Antum crater is marked by dark-rayed ejecta that obscure older features and reshape the surrounding landscape. This study investigates Antum and its geological context using optical and infrared data from the Voyager and Galileo missions, complemented by numerical simulations. The terrain around Antum can be divided into three facies based on albedo and texture, reflecting a complex history shaped by impact and resurfacing. Galileo/NIMS spectra reveal sharp contrasts between the crater interior and its ejecta: the interior shows deeper water ice absorption bands, while the ejecta appear darker and more contaminated. Spectral features also indicate salts, complexed CO_2, and hydrated sulfuric acid, pointing to subsurface alteration and cumulative space weathering. Numerical simulations of the cratering process with the iSALE-2D code highlight the influence of impact velocity, thermal gradients, and surface cohesion on crater formation. Under plausible impact conditions, the modeled crater dimension and morphology closely match observations, offering insight into the processes controlling cratering on icy surfaces. By integrating geological mapping, Galileo/NIMS spectral analysis, and impact modeling, this study refines our understanding of Ganymede's geological evolution. The results suggest past or present subsurface liquid activity and highlight the mechanisms that shape icy moons. Antum thus represents a key case study with broader implications for planetary science and the evolution of outer Solar System bodies, and its investigation is also relevant for upcoming missions such as JUICE and Europa Clipper.

Plain Language Summary This study explores the Antum Crater on Ganymede, Jupiter's largest moon, and its surrounding landscape. Data from past space missions, along with modern techniques, were used to understand how the crater and its region formed and evolved. The dark debris from the crater has covered older surface features, showing how powerful impacts can reshape the moon's landscape. The surrounding area is divided into different zones based on texture and brightness, which tell the story of Ganymede's geological history. One of the main findings is that the interior of the crater has more water ice, while the debris thrown out by the impact contains dark, mixed materials, including salts, carbon dioxide, and sulfuric acid. These materials suggest that subsurface processes may have occurred, and that the region has been exposed to environmental changes over time. Computer simulations of the crater's formation also help explain how impacts shape these terrains. This research offers new insights into the history and potential activity of icy moons such as Ganymede. It helps improve understanding not only of Ganymede's evolution, but also of the broader processes that might shape other icy moons in the outer Solar System.

Key Points:

- Antum's formation by hypervelocity impact exposes Ganymede's icy crust, reshaping its surface and revealing geological processes
- Ejecta's varied makeup, with hydrated salts and CO_2, suggests impact-driven chemistry and possible brine mobilization
- Antum's study highlights impact-driven resurfacing and chemical evolution, offering insights into icy moon dynamics and potential habitability

Supporting Information:

Supporting Information may be found in the online version of this article.

Correspondence to:

F. Tosi,
federico.tosi@inaf.it

Citation:

Tosi, F., Colaiuta, F., Galluzzi, V., Martellato, E., Zambon, F., Stephan, K., et al. (2025). Antum crater: A window into Ganymede's icy evolution. *Journal of Geophysical Research: Planets*, *130*, e2025JE009202. https://doi.org/10.1029/2025JE009202

Received 22 MAY 2025
Accepted 7 SEP 2025
Corrected 11 NOV 2025

This article was corrected on 11 NOV 2025. See the end of the full text for details.

Author Contributions:

Conceptualization: Federico Tosi
Formal analysis: Federico Colaiuta, Valentina Galluzzi, Elena Martellato, Francesca Zambon
Investigation: Federico Colaiuta, Valentina Galluzzi, Elena Martellato, Francesca Zambon
Methodology: Federico Tosi, Federico Colaiuta, Valentina Galluzzi, Elena Martellato, Francesca Zambon
Project administration: Federico Tosi
Software: Federico Colaiuta, Francesca Zambon

1. Introduction

Ganymede, Jupiter's largest moon, features an icy crust that contains a rich array of geological formations, each providing insight into its long and complex history. Among the most fascinating and enigmatic geological features on Ganymede's surface are the *Dark Ray Craters* (DRCs), namely craters with a low-albedo ejecta blanket. The Near Infrared Mapping Spectrometer (NIMS) aboard NASA's Galileo mission (Carlson et al., 1992) acquired data for the DRCs Kittu, Mir, and Antum at comparable spatial resolutions: approximately 3.0, 3.4, and 2.1 km/pixel, respectively. NIMS data demonstrated that DRCs are not a uniform compositional group, with many resulting from the excavation of darker Ganymede hydrate material, in some cases mixed with a less hydrated, non-ice material that may represent a remnant of the impactor body (Hibbitts, 2023; Stephan et al., 2025). The

Supervision: Federico Tosi
Visualization: Federico Colaiuta, Valentina Galluzzi, Elena Martellato
Writing – original draft: Federico Tosi, Federico Colaiuta, Valentina Galluzzi, Elena Martellato
Writing – review & editing: Federico Tosi, Katrin Stephan, Namitha R. Baby, Lorenzo Bruzzone, Pasquale Palumbo, Giuseppe Piccioni

dark rays in these craters may also indicate interactions between the ice and chemical components from the outer Solar System, potentially delivered by comets or carbonaceous asteroids. Space weathering could significantly influence the compositional evolution of these craters. Unlike Europa and Callisto, Ganymede's surface preserves these craters and rays over extended geological timescales, due to its intrinsic magnetic field.

This study aims to understand the formation and evolution of Antum Crater, focusing on its geological, spectral, and impact dynamics. Antum, located at ∼5.1°N, 218.9°W (141.1°E) in Marius Regio on Ganymede's anti-Jovian, trailing quadrant, is an impact crater ∼15 km in diameter as measured from its inner dark ring (our study will explore a revised value based on an accurate geologic mapping and comparison with NIMS data). Unfortunately, unlike the Kittu crater, high-resolution Galileo optical images of Antum are unavailable. The most relevant contextual images are those obtained from the Voyager mission. The interior and rim of the crater are predominantly bright although the low resolution prevents definitive identification of whether the crater has a peak or a pit. These dark rays are believed to be discontinuous ejecta, forming a thin overlay of dark material upon the underlying terrain of Marius Regio.

The Voyager mission first captured images of Antum with a resolution of about 2 km per pixel, and it was subsequently observed at the same resolution by the Galileo/NIMS instrument, which is exceptionally high for the NIMS data set and serves as the foundation of this study. The prominent morphological features and albedo variations observed in the images suggest that Antum is a relatively young impact crater. This is corroborated by the band depth map of water ice absorption at 1.5 μm derived from NIMS data, which shows an enrichment of water ice in the crater and dark non-ice material in the surrounding rays (Baby et al., 2024). The distribution of concentrated dark non-ice material corresponds to the dark rays seen in the camera images. Bright and dark terrains in the Antum area indicate water ice grain sizes ranging from 1 to 2 mm (Baby et al., 2024), which correlate with global variations in grain size as a function of Ganymede's surface temperature, as described by Stephan et al. (2020). The primary geological features of Antum include a distinct crater floor and rim, continuous bright ejecta, and extensive dark rays. Unlike Kittu and Mir, no correlation between water ice and CO_2 abundance is observed in Antum (Hibbitts et al., 2003). According to a spectral unmixing model, the dark ejecta associated with Antum may comprise one of the highest concentrations of dark material (approximately 50%) on Ganymede, with near-infrared reflectance approaching 20% (Hibbitts, 2023) and mostly represent redistributed dark terrain material (Baby et al., 2024). Impact modeling suggests that the maximum excavation depth in Antum may range between 1.2 and 2.3 km (Baby et al., 2024).

Section 2 presents a detailed geological mapping of the Antum crater region. Using a controlled Ganymede mosaic as a basemap, we identify and classify terrain units based on albedo and texture. The crater rim is mapped at a diameter of 25 km, rather than the previously reported 15 km. The study indicates that the impact event that created Antum significantly altered the surrounding landscape, with asymmetric ejecta suggesting an impact direction from south-southeast to north-northwest.

Section 3 presents a comprehensive reanalysis of Galileo/NIMS data to enhance our understanding of the surface composition in the impact region. We use various spectral indices to map the contributions of water ice and non-ice contaminants. Additionally, we applied both linear and non-linear spectral unmixing models to identify the most likely spectral endmembers and determine their abundances.

The impact that formed Antum has distinctly modified the region, generating unique ejecta layers and post-impact alterations in the landscape. Section 4 highlights iSALE-2D simulations of the Antum crater on Ganymede, testing different impact velocities (20–10 km/s) and projectile sizes (600–750 m). These simulations yield a crater diameter of ∼25 km, with no prominent central peak and distinct ejecta patterns. The role of thermal gradients and surface cohesion is also investigated, revealing that both smaller thermal gradients and higher cohesion result in a deeper craters.

Research into DRCs is set to remain a key focus, especially with upcoming space missions to Ganymede like JUICE (Stephan, Roatsch, et al., 2021). This case study provides valuable insights for the future planning of Antum observations by all remote sensing instruments aboard JUICE, which may help elucidate the origin of the crater and its relationship to both the subsurface and other DRCs.

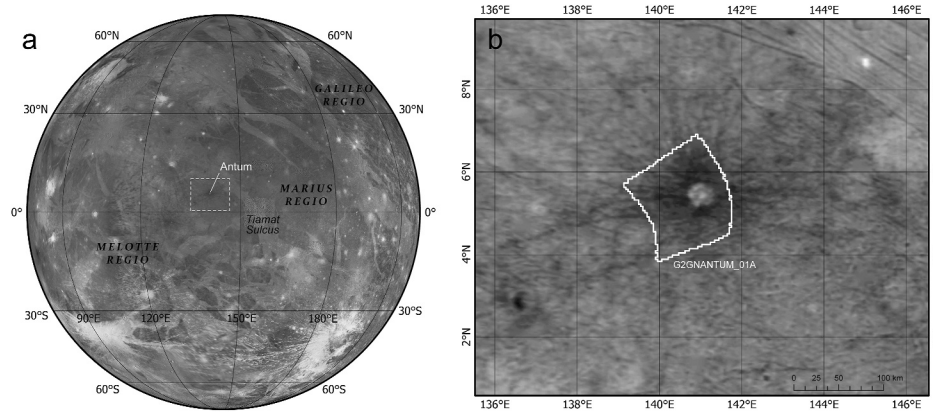

Figure 1. (a) Antum Crater Region (ACR) on Ganymede and (b) overview of the Antum crater and contour of NIMS data covering this region. The optical basemap is from Kersten et al. (2021).

2. Geological Framework of the Antum Crater Region

2.1. Description

The Antum Crater area spans longitudes 135.3°E to 146.7°E and latitudes 9.8°N to 0.5°N (Figure 1). It lies within the western part of Marius Regio, directly west of Tiamat Sulcus. This region closely resembles Marius Regio in its general appearance, yet it is predominantly characterized by the dark-rayed ejecta of Antum crater, which largely obscure older geological features typical of the area, such as ancient concentric rings. Antum crater, being the largest dark-rayed crater in the region with sufficient basemap detail, serves as the focal point of this study. In the following section, we refer to this area as the "*Antum Crater Region* (ACR)."

Previous studies have conducted geological analyses of the region using either Voyager imagery, achieving a pixel resolution of ~2 km (Figure 2a, Croft et al., 1994; Guest et al., 1988) or a combination of Voyager/Galileo imagery (Figures 2b, Collins et al., 2013; Patterson et al., 2010). Geological mapping based on Voyager data comprises a series of quadrangle maps at a 1:5,000,000 scale. The ACR analyzed here is situated at the boundary between two quadrangles: (a) the Tiamat Sulcus quadrangle (Jg-9, Croft et al., 1994), and (b) the Uruk Sulcus quadrangle (Jg-8, Guest et al., 1988). These maps provide a high level of detail, allowing the identification of craters as small as 20 km in diameter, with Antum being the smallest identified crater. They also exhibit a strong correspondence in contacts and geological units across quadrangle boundaries (Figure 2a). In contrast, the global geological map of Ganymede, created using Voyager and Galileo data (Collins et al., 2013; Patterson et al., 2010),

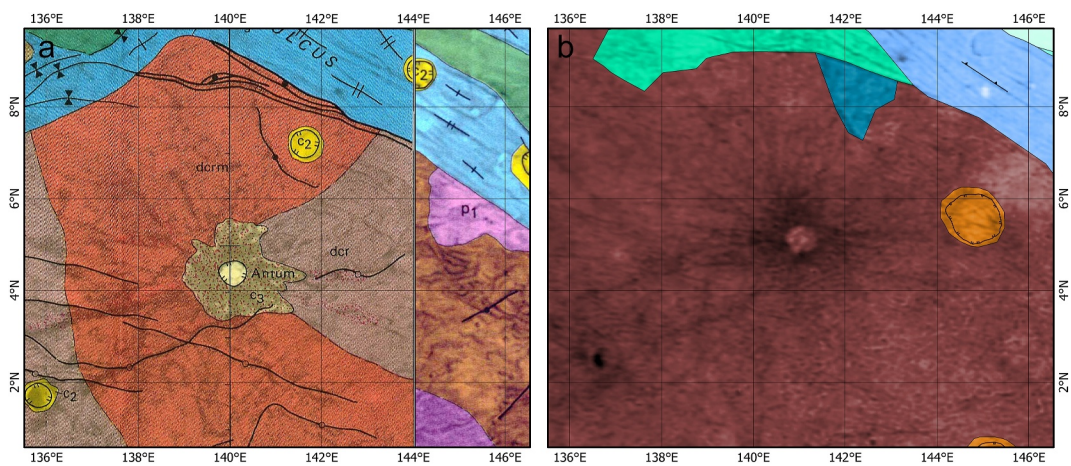

Figure 2. Geological maps of ACR: (a) Reprojected quadrangles from the Voyager-based geological mapping campaigns of Jg-9 (left, Croft et al., 1994) and Jg-8 (right, Guest et al., 1988). (b) Voyager/Galileo-based global geological map of Ganymede (Collins et al., 2013).

provides a more regional, 1:15,000,000-scale view of the area, but lacks the finer detail needed to identify smaller features, such as Antum crater (Figure 2b).

While Baby et al. (2024) offer additional details on Antum crater itself, information on the surrounding geological context remains sparse. To fully understand the evolution of Antum crater, we propose a comprehensive geological study that integrates all prior geological maps and synthesizes interpretations from various works, including those by Guest et al. (1988), Croft et al. (1994), Patterson et al. (2010), Collins et al. (2013), and Baby et al. (2024). This approach provides a more coherent stratigraphic framework for the dark-rayed ejecta of Antum crater and allows for direct comparison with the NIMS data, which precisely targets the crater floor and its proximal ejecta.

2.2. Data and Methods

We use the controlled global Ganymede mosaic at 359 m/pixel from Voyager and Galileo images as the primary basemap reference (Kersten et al., 2021). Such a "controlled mosaic" is an image mosaic in which individual frames are geometrically aligned to each other and tied to a planetary coordinate system through ground control points, ensuring accurate spatial referencing for geological mapping. Due to the absence of higher-resolution Galileo Solid-State Imaging (SSI) frames in this region, we maximized the stretch of the available basemap to enhance spatial detail.

Following USGS planetary mapping guidelines (Skinner et al., 2018), we employ symbology recommended by the Federal Geographic Data Committee (FGDC) for planetary geological maps. The linework was created at a scale of approximately 1:1,000,000, which is consistent with an output scale of 1:5,000,000, comparable to the Voyager geological maps (Croft et al., 1994; Guest et al., 1988).

Our geological investigation follows a morpho-stratigraphic approach, classifying geological units based on their albedo and texture. Undivided crater materials are grouped into three degradation classes (*c1* to *c3*), ranging from the most degraded to the freshest craters, in line with previous studies. We utilize two types of geological contacts (certain and approximate) and include various linear features to represent prominent morphological characteristics. Notably, troughs within the sulci are delineated where they are most prominent.

2.3. Geological Mapping

The geological map presented in Figure 3 outlines various terrain units, sulcus units, and crater materials in the ACR. The oldest unit is represented by dark, rough terrains of Marius Regio, which are further divided into three facies based on albedo and texture. The first facies (*rt1*) is characterized by a dark albedo with denser lineaments and fracturing compared to the surrounding terrain. The second facies (*rt2*) exhibits a slightly brighter albedo with sparser lineaments, though the texture remains similar to that of rt1. The third facies (*rt3*) features an even brighter albedo although it is present only in discontinuous patches. Sulcus units, mainly associated with Tiamat Sulcus, were identified based on their morphology, albedo, and groove systematicity. The primary sulcus unit (*sT*) is moderately bright, smooth, and systematically grooved. The peripheral parts of Tiamat Sulcus (*sT1*) lack systematic grooves but can be distinguished from the surrounding terrain by their smooth morphology and brighter albedo. The groove systematicity persists beyond Tiamat Sulcus on the rt1 facies.

For Antum, we mapped the rim crest at the boundary of maximum albedo contrast between its ejecta and the inner floor. This leads to a rim extent of 25 km, in contrast to previous estimates which suggested a rim of 15 km based on the inner dark ring. However, we mapped a rim unit (*Ar*) that could encompass the rim crest across its extent to account for uncertainties due to the resolution limits of the basemap. The inner structure of Antum displays a bright circular feature at its center (*Ac*), possibly (but not necessarily) indicating a central dome. Surrounding this is a darker unit interpreted as the original crater floor (*Af*). An extreme stretch of the basemap allowed the distinction of three dark ejecta facies based on albedo (*Ae1* to *Ae3*, from the darkest and proximal to the least dark and distal), which may facilitate comparisons with NIMS data. For stratigraphic correlation, the distal portion of the Tammuz dark ejecta rays (*Te*) was mapped, which appear to be older than the Antum dark rays, despite resolution limitations.

Finally, the mapping area includes two palimpsest-like features (*pc*), one of which is classified as uncertain (*pcu*) due to insufficient resolution and its overlap with the sT1 bright unit. In the geological map by Collins et al. (2013), the confirmed palimpsest-like feature (*pc*) was identified as a c1 crater (i.e., the oldest class of

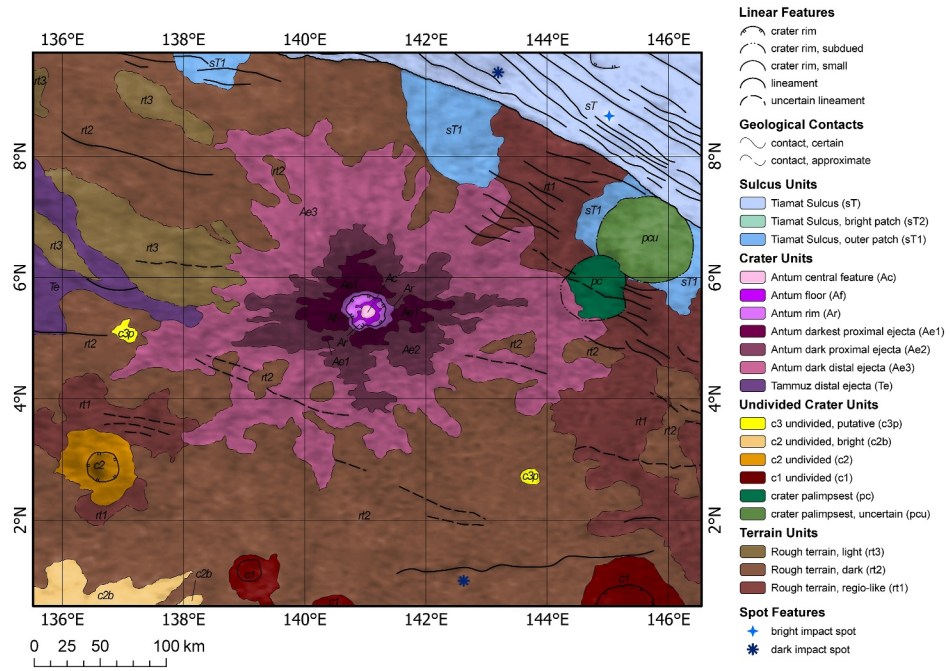

Figure 3. Geological map of the Antum Crater Region. Units are blended in overlay-mode over the Ganymede controlled basemap (Kersten et al., 2021) to enhance transparency of the basemap albedo contrasts.

craters). However, our previous mapping experience with palimpsest features suggests that subdued morphology alone is not sufficient to infer an ancient origin for these structures (see the case of Epigeus in Tosi et al., 2023).

3. Spectroscopic Analysis

3.1. Spectral Indices

We now focus on one hyperspectral image obtained by Galileo/NIMS on the Antum crater region (hyperspectral image *G2GNANTUM*_01A. The data set represents the highest spatial resolution ever achieved by NIMS on Ganymede (~2 km/pixel), and one of the highest resolutions ever obtained for the icy Galilean moons. The data, calibrated in units of I/F, was photometrically corrected using the Akimov disk function (Shkuratov et al., 1999) and smoothed with a Savitzky-Golay filter to reduce spurious effects such as radiation-induced spikes or high-energy particle noise. Figure 4 presents the average spectral profile for this hyperspectral image, along with the data's dispersion.

To gain a preliminary understanding of contaminant distribution and water ice grain size, we calculated spectral indices based on the reflectance spectra (see Text S1 in Supporting Information S1). Specifically, we computed band depth values for water ice features at 1.25, 1.50 and 2.00 μm, and for the carbon dioxide feature at 4.25 μm (Figure 5). The band depth for the 2-μm feature was calculated considering the wavelength position of the band center (Figure 6c). Analysis of the band depths for water ice (Figures 5a–5c) reveals a spatial distribution typical of DRCs. Reduced water ice band depth values in dark ejecta indicate a higher concentration of contaminants such as hydrated salts (Stephan et al., 2020), or alternatively, smaller water ice grains compared to the crater floor. Additionally, the crater floor is compositionally distinct in two areas: one with higher band depth values, designated *Crater Floor 1* (CF1), and another with lower values, labeled *Crater Floor 2* (CF2). Another significant absorption feature is observed at 4.25 μm (Figure 5d), associated with complexed CO_2. At a regional scale, this signature is stronger at low latitudes than at high latitudes (Bockelée-Morvan et al., 2024).

The average value of the 4.25-μm band depth is approximately 0.22, consistent with previous studies (Bockelée-Morvan et al., 2024). However, specific locations within the image show larger 4.25-μm band depth values, possibly related to a higher concentration of complexed CO_2. To further investigate the distribution of contaminants and water ice grain size, we calculated additional spectral indices based on previous work on icy

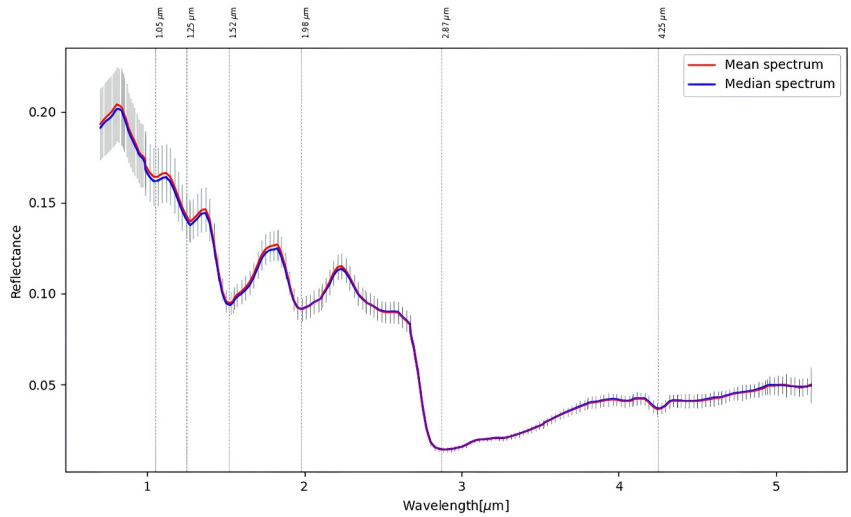

Figure 4. Mean and median spectra of the Antum Crater Region, after applying the Akimov disk function and smoothing. Grey bars represent the 1-σ dispersion of the data within the G2GNANTUM_01A hyperspectral image. Instrumental uncertainties are smaller than the data dispersion (see Supporting Information S1). The close similarity between the mean and median spectra indicates that the data distribution is largely symmetric. Absorption bands are marked by vertical dashed lines. We do not discuss the 1.05 and 2.87 μm bands due to calibration residuals near the 1-μm region and challenges in identifying the right shoulder of the 2.87-μm water band, respectively.

satellites (Filacchione et al., 2012; Tosi et al., 2023, see Text S1 in Supporting Information S1). First, we derived a spectral slope between 1.10 and 2.24 μm (Figure 6a). Small absolute values of this spectral slope suggest fine water ice grains, while large values indicate coarser grains. The 3.60/1.82 μm reflectance ratio also serves as an indicator of water ice grain size, with smaller values of the ratio indicative of larger grains. This confirms the presence of large water ice grains in the crater floor and fine grains in the dark ejecta (Figure 6b).

To further explore the distribution of darkening agents in the ACR, we evaluated the center and asymmetry of the 2-μm water ice absorption band, following Scipioni et al. (2017) (see Supporting Information S1). Our findings indicate that dark ejecta exhibit a shift of the 2-μm band to slightly shorter wavelengths (Figure 6c), with asymmetry parameter values exceeding unity (Figure 6d). This shift could result from the presence of either hydrated salts (Stephan et al., 2020) or amorphous ice (Mastrapa et al., 2008). Given Ganymede's intrinsic magnetic field, which preserves crystalline water ice from radiation at low latitudes (Liuzzo et al., 2020), combined with typical daytime surface temperatures at low latitudes (Ligier et al., 2019; Orton et al., 1996), we rule out amorphous ice as a potential explanation.

By comparing spectral indices with our geological map (Figure 7), we find that the units along the Antum crater rim (primarily corresponding to CF1) align with an area depleted in contaminants, displaying a deeper 2-μm water ice absorption band (Figure 5b). This supports the hypothesis that the actual size of the excavated crater is closer to 25 km rather than the 15-km value reported in the IAU database. Additionally, an obvious spatial correlation exists between the Ae1 crater unit and the magenta areas in Figure 7b, indicating dark terrain units characterized by a shallower 2-μm water ice absorption band and smaller ice grain sizes. This correspondence aligns with expectations for a region influenced by material redistribution following the impact, with a slight extension of the ejecta toward the north-northwest.

Based on the morphology and spectral variability revealed by the maps in Figures 5 and 6, six regions of interest (ROIs) were selected within the NIMS G2GNANTUM_01A image (Figure 8). These include CF1 and CF2 in the crater floor, DE1 and DE2 (Dark Ejecta 1 and Dark Ejecta 2) in distinct areas of the dark ejecta, and OR1 and OR2 (Other Region 1 and Other Region 2), which are far enough away from the impact site to be considered marginally affected by post-impact material redistribution. With regard to the ROIs located on the crater floor, CF1 and CF2 were delineated based on observed variability in water-ice abundance and grain size. This variability, highlighted by the differences in band depths shown in Figures 5a–5c, suggests a relatively higher abundance of water ice and/or the presence of coarser grains in CF1 compared to CF2. In addition, DE1 and DE2 were defined to assess

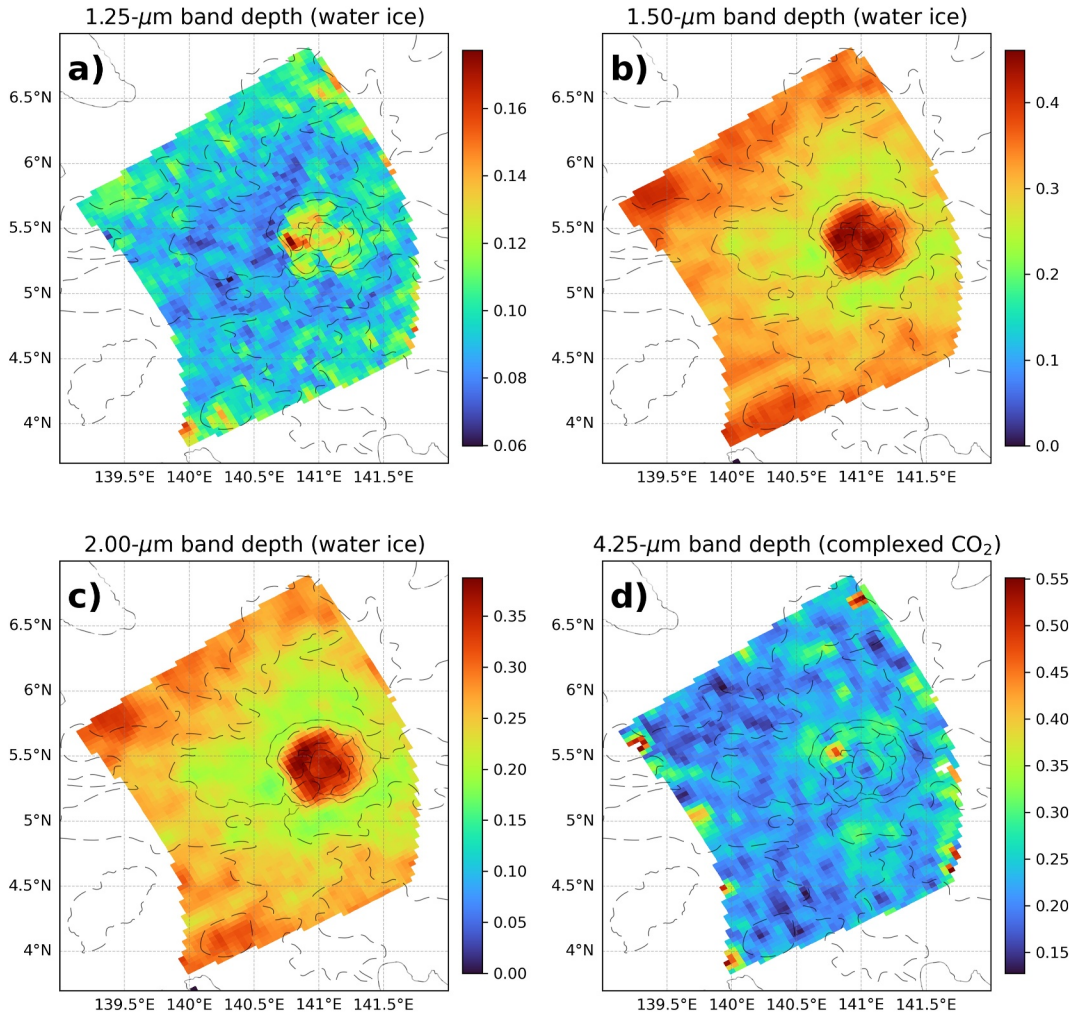

Figure 5. Band depth values obtained for different spectral features in the NIMS hyperspectral image G2GNANTUM_01A: (a) 1.25 μm, (b) 1.50 μm, (c) 2.00 μm, and (d) 4.25 μm. The spatial distribution of these indices reveals compositional differences among three main regions: the crater floor, dark ejecta, and outer regions. To facilitate comparison, the geological units mapped in Figure 3 are overlaid with dashed grey contours.

potential variations in salt content along different directions, taking into account the distribution of ejecta illustrated in Figure 7a.

To further investigate water ice grain size in these ROIs, we computed specific band depth ratios (BDR) (Stephan et al., 2020): BDR1 (2.00/1.50 μm), BDR2 (2.00/1.25 μm), and BDR3 (1.50/1.25 μm) (Table 1). These ratios were compared to those predicted for water ice and a linear mixture of water ice and epsomite ($MgSO_4 \cdot 7H_2O$), a hydrated mineral salt with spectral characteristics similar to those of water ice.

Figure 9 aids in estimating the water ice grain size in the presence of hydrated non-ice contaminants. BDR1 values ranging from 0.77 to 0.86 suggest that grain sizes within the Antum crater may reach up to one mm or more, consistent with previous investigation of Antum by Baby et al. (2024) and broader studies on spatial grain size distribution on Ganymede (King & Fletcher, 2022; Stephan et al., 2020). BDR2 indicates that grain sizes in the dark ejecta are smaller than 1 mm, with diameters decreasing to approximately 200 μm. BDR3 displays considerable variation in grain sizes, ranging from a few hundred microns to a few thousand microns. Overall, water ice grain sizes in the ACR vary between 50 and 3,000 μm, with notable differences between the crater floor and the surrounding regions. This variation implies that, even within the dark ejecta, water ice grains may reach up to one mm, although they are generally smaller than those found on the crater floor. This distinction is expected, as dark ejecta predominantly consist of surface materials redistributed by impact, possibly including hydrated

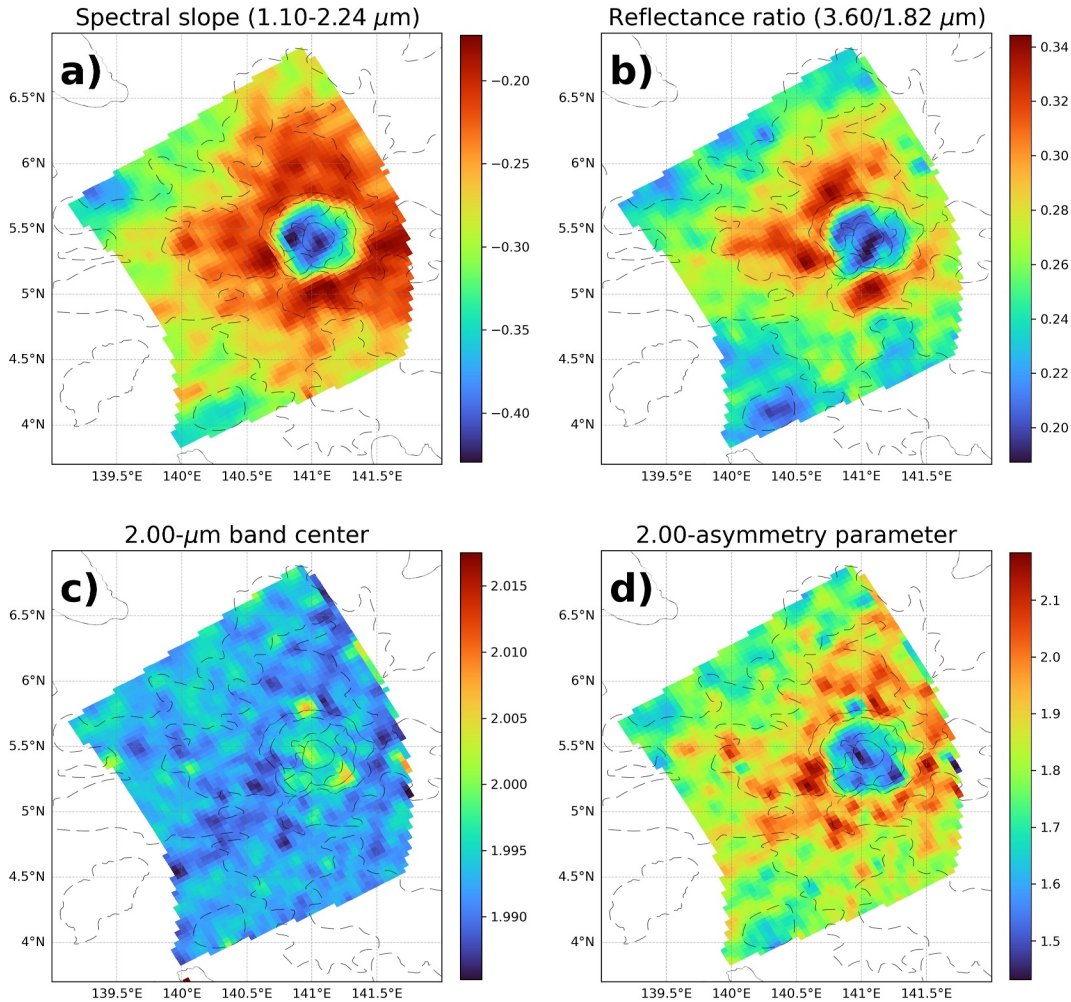

Figure 6. (a) Spectral slope (1.10–2.24 μm), (b) reflectance ratio (3.60/1.82 μm), (c) band center (2-μm), and (d) asymmetry parameter at 2 μm. These indices provide insight into water ice grain size and non-ice contaminant distribution. Dark ejecta are expected to have higher abundances of hydrated salts, suggested by a shift toward shorter wavelengths in the 2-μm band, as shown in panels (c, d). To facilitate comparison, the geological units mapped in Figure 3 are overlaid with dashed grey contours.

salts and other contaminants, whereas the crater floor exposes a subsurface layer. Protected from space weathering and sublimation, this subsurface layer has allowed for the growth of larger ice grains over time. The impact event likely caused partial sublimation of surface ice grains due to the thermal energy released, resulting in smaller ice grains in the dark ejecta compared to those in deeper subsurface layers.

When interpreting water ice grain sizes, the distribution of carbon dioxide in the region can be examined through spectral index analysis. The depth of the 4.25-μm band (Figure 5d) and the RGB color composite map (Figure 8c) indicate the presence of carbon dioxide in the area; however, no direct correlation is observed with the various terrain types, suggesting that the abundance of CO_2 in the Antum crater is similar to that of the nearby terrain (Hibbitts et al., 2003).

3.2. Linear Spectral Unmixing: FCLS and MCMC

We employed linear spectral unmixing using two methods: Fully Constrained Least Squares (FCLS) (Bioucas-Dias & Figueiredo, 2010) and Markov Chain Monte Carlo (MCMC) (Speagle, 2020). FCLS applies a least squares approach to combine spectral endmembers linearly, with coefficients indicative of their relative abundances. This method is computationally efficient, allowing its application on a pixel-by-pixel basis across the

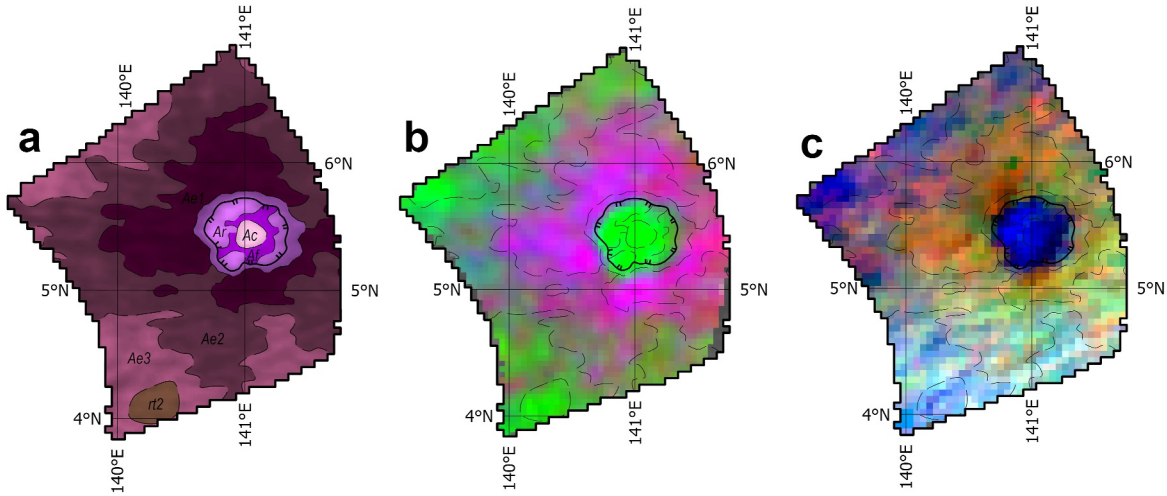

Figure 7. (a) Portion of the geological map from Figure 3 (refer to the legend); (b) RGB color composite from spectral indices (R = spectral slope 1.10–2.24 μm, G = band depth at 2 μm, B = reflectance ratio 3.60/1.82 μm) and (c) RGB color composite from reflectance values (R = 4.25 μm, G = 2.00 μm, B = 1.25 μm).

entire study area and the generation of spatially resolved maps. However, its uncertainty estimates are less rigorous than those obtained with alternative approaches, since they are based on bootstrap resampling and would require an exceedingly large number of iterations to yield statistically robust confidence intervals. In contrast, MCMC directly samples the posterior parameter distribution, progressively refining the estimates and providing more rigorous and robust uncertainty quantification. Nevertheless, the substantial computational demands of MCMC limited its application in this study to the six selected ROIs, precluding its use on the full NIMS image as done with FCLS. Despite these differences, the combined application of the two methods has been successfully employed in previous studies of Ganymede's surface composition, enabling the detection of specific compounds such as salts and organics (e.g., Tosi, Mura, et al., 2024).

Initially, FCLS and MCMC were applied to analyze the distribution of water ice grain sizes across the ACR, using laboratory-measured spectral profiles of water ice at various grain sizes, alongside two synthetic spectra, labeled "black" and "white," with constant values of 0.0 and 1.0, respectively. These flat spectra account for differences in reflectance values between the NIMS data and laboratory spectra. Given that the main goal was to assess water ice grain size, we focused on the 1.0–2.5 μm spectral range, where the diagnostic absorption bands of water ice do not saturate in the laboratory data (Stephan, Ciarniello, et al., 2021). Both methods identified two primary

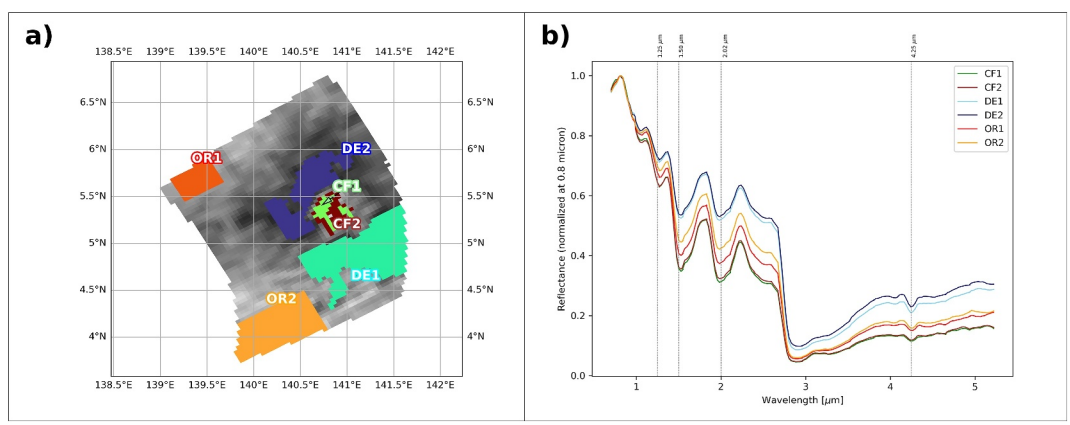

Figure 8. Spectral index analysis of the G2GNANTUM_01A data set. (a) Spatial distribution of the identified regions of interest (ROIs), overlaid on a 2.0-μm background image that highlights the contrast between water-ice-rich and salt-rich terrains. (b) Average spectral profiles of the ROIs (normalized at 0.8 μm), colored by type: CF1 (green), CF2 (burgundy), DE1 (aqua), DE2 (midnight blue), OR1 (red), and OR2 (orange). Diagnostic absorption bands are indicated at ∼1.25, ∼1.50, and ∼2.00 μm (water ice) and ∼4.25 μm (complexed CO_2).

Table 1
Average Band Depth Ratios Computed for Each Regions of Interest

BDR	CF1	CF2	DE1	DE2	OR1	OR2
1	0.86 ± 0.01	0.83 ± 0.01	0.78 ± 0.01	0.77 ± 0.01	0.81 ± 0.01	0.80 ± 0.01
2	2.89 ± 0.01	2.84 ± 0.01	2.35 ± 0.01	2.45 ± 0.01	2.91 ± 0.01	2.83 ± 0.01
3	3.38 ± 0.01	3.43 ± 0.01	3.01 ± 0.01	3.18 ± 0.01	3.58 ± 0.01	3.52 ± 0.01

Note. BDR1 (2.00 μm/1.50 μm), BDR2 (2.00 μm/1.25 μm) and BDR3 (1.50 μm/1.25 μm) are showed respectively in the first, second, and third row of the table. For each ROI, these values are compared to the trends presented in Figure 9.

endmembers, water ice with grain sizes of 70 and 1,360 μm, as key contributors to reconstructing the average spectral profile for each ROI.

The distribution of water ice grains obtained via FCLS indicates that the Antum crater corresponds to a depletion of fine grains and an enrichment of coarse grains (Figures 10a and 10d). This sharp contrast in grain size may be linked to the physical properties of the subsurface layer excavated by the impact. Additionally, intermediate grain sizes, notably 200 and 300 μm, are also observed in the ACR (Figures 10b and 10c), suggesting post-impact processes such as mass wasting or deeper excavation in certain areas. The water ice grain maps also suggest that dark ejecta are best represented by a combination of 70-μm and 200-μm grains, indicating fine material, which aligns with our previous findings based on spectral indices (Figure 6). On the other hand, water ice grains at 680 and 1,060 μm provide no statistically meaningful contribution in the linear combination.

Relying on the spectral library presented in Table S1 of Supporting Information S1, besides water ice, the optimal endmembers identified for various compound categories include: ammonia ice (NH_3, among volatiles), bloedite ($Na_2Mg(SO_4)_2{\cdot}4H_2O$, among sulfates), hydrohalite ($NaCl{\cdot}2H_2O$, among chlorides), burkeite ($Na_6(CO_3)(SO_4)_2$, among carbonates), ammonium nitrate (NH_4NO_4, among nitrates), and asphaltite (among organics). This does not imply the presence of ammonia ice, burkeite, ammonium nitrate, or asphaltite (furthermore, ammonia ice could not survive the surface temperatures typical of Ganymede); but indicates that, within each category, these endmembers are the most suitable for modeling the spectral profiles observed by NIMS.

Both the FCLS and MCMC methods fail to identify carbon dioxide as the primary endmember for volatiles other than water, despite its presence on Ganymede being well-established by previous spectroscopic studies (e.g., Bockelée-Morvan et al., 2024; Hibbitts et al., 2003) and by our own preliminary spectral analysis (Figures 5d and 7c). This may be due to the use of CO_2 ice in our spectral library, whereas on Ganymede, CO_2 is primarily complexed with water ice in the uppermost surface layer, which alters its spectral shape. Furthermore, the limited number of points identifying the 4.25-μm band and the broad spectral range used in the simulations constrain the method's ability to efficiently model the signature of this compound. Exogenous compounds and phosphates show negligible contributions in the linear combination, as their associated scalar coefficients are comparable to statistical noise. These results were cross-checked using both FCLS and MCMC methods across the six ROIs. While

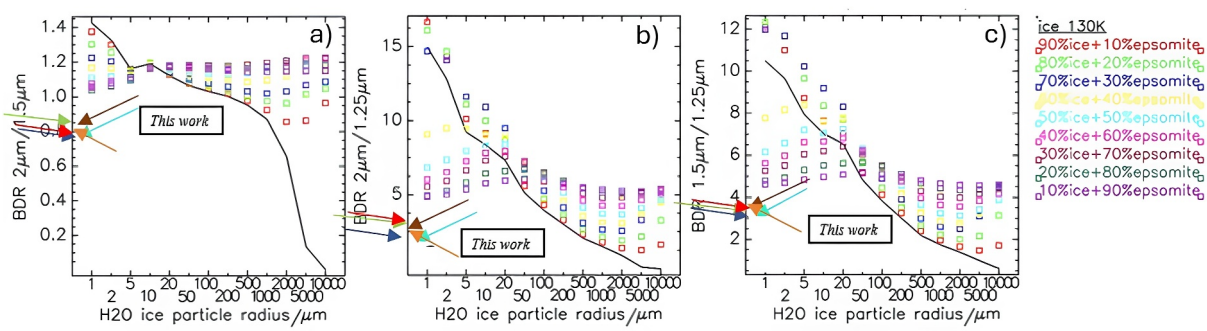

Figure 9. Band depth ratios (BDR) values computed for regions of interest identified in the Antum Crater Region, compared to the BDR versus water ice grain size as found in Figure 6 (panels d–f) of Stephan et al. (2020). Each panel illustrates a specific BDR as a function of water ice grain size, assuming either pure water ice (solid black line) or a linear combination of water ice and epsomite (colored squares). (a) BDR1, (b) BDR2, (c) BDR3. The colored arrows pointing to the *y*-axis of each plot indicate the specific BDR value obtained for the ROIs: CF1 (green), CF2 (burgundy), DE1 (aqua), DE2 (midnight blue), OR1 (red) and OR2 (orange).

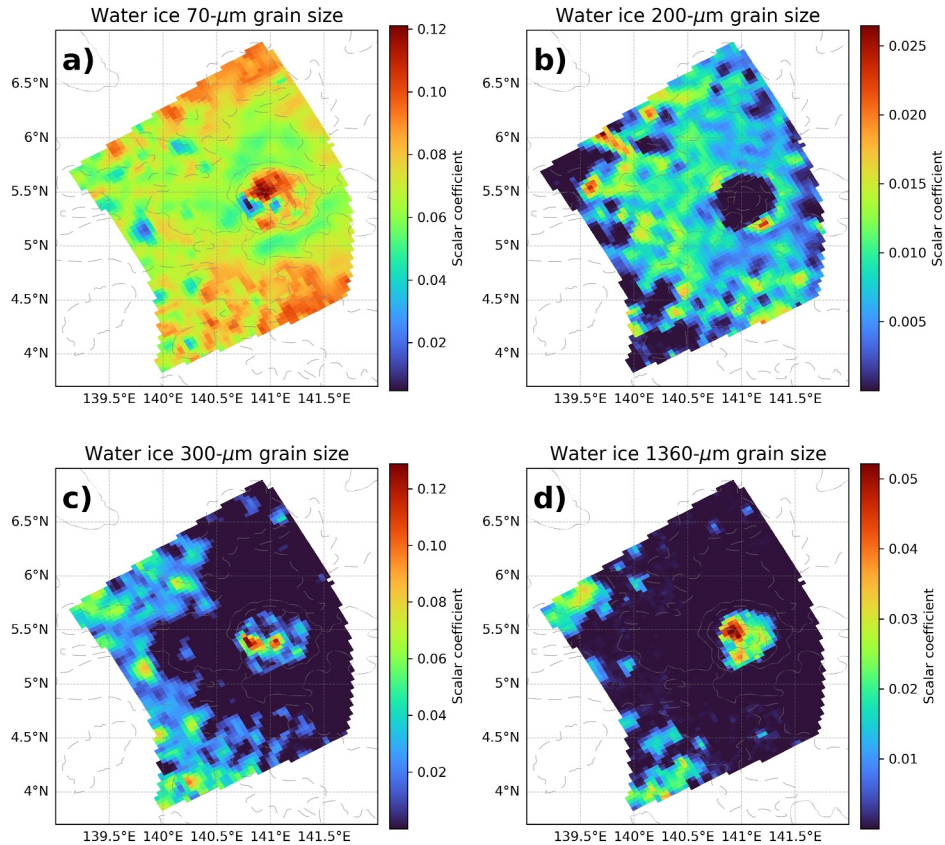

Figure 10. Spatial distribution of water-ice grain sizes and flat, featureless spectra in the ACR: (a) 70-μm, (b) 200-μm, (c) 300-μm, and (d) 1360-μm grain sizes. In each panel, the color bar indicates the scalar coefficient value derived from Fully Constrained Least Squares spectral unmixing, which reflects the relative abundance of the corresponding water-ice endmember. To facilitate comparison, the geological units mapped in Figure 3 are overlaid with dashed grey contours.

the results of both models are consistent within their respective uncertainties, FCLS enables pixel-by-pixel mapping of endmember contributions across the entire ACR. This spatial coverage facilitates the identification of potential correlations with underlying geological units (see the geological unit boundaries overlaid onto the spectral maps in Figures 5, 6, 10 and 11). While MCMC could, in principle, support a similar analysis, sampling the posterior distribution with multiple chains leads to slow numerical convergence and prohibitively high computation times for each pixel, making it impractical for full-scene mapping. Moreover, the MCMC model tends to systematically overestimate the contribution of asphaltite compared to FCLS (Tables 2 and 3), producing results that are inconsistent with the observed spectral characteristics. Therefore, despite providing less rigorous uncertainty quantification than a fully statistical approach such as MCMC, FCLS emerges as the more reliable and computationally efficient solution for linear unmixing in this study.

For the subsequent simulation, we considered a mixture of the best endmembers identified within each category, plus water ice with grain sizes of 70 and 1360 μm, and the two flat "black" and "white" spectra, and carried out the simulation over the 1.00–4.75 μm spectral range.

Our results show that the contribution of water ice in the crater floor is significantly greater than that in the dark ejecta (Tables 2 and 3). Additionally, the contribution of coarse-grained water ice is higher in CF1 than in CF2, reinforcing previous findings from spectral indices. Conversely, a generally larger contribution of salts is observed in the dark ejecta, likely due to the redistribution of surface materials following the impact event. For example, hydrohalite may be compatible with liquid extrusion from subsurface slush. Non-negligible coefficients for ammonium nitrate may be linked to the possible presence of ammoniated salts. The high coefficient values found for asphaltite in all ROIs may be an artifact due to the featureless profile of asphaltite at short wavelengths, with organic compounds displaying their diagnostic signatures between 3 and 4 μm in the near infrared.

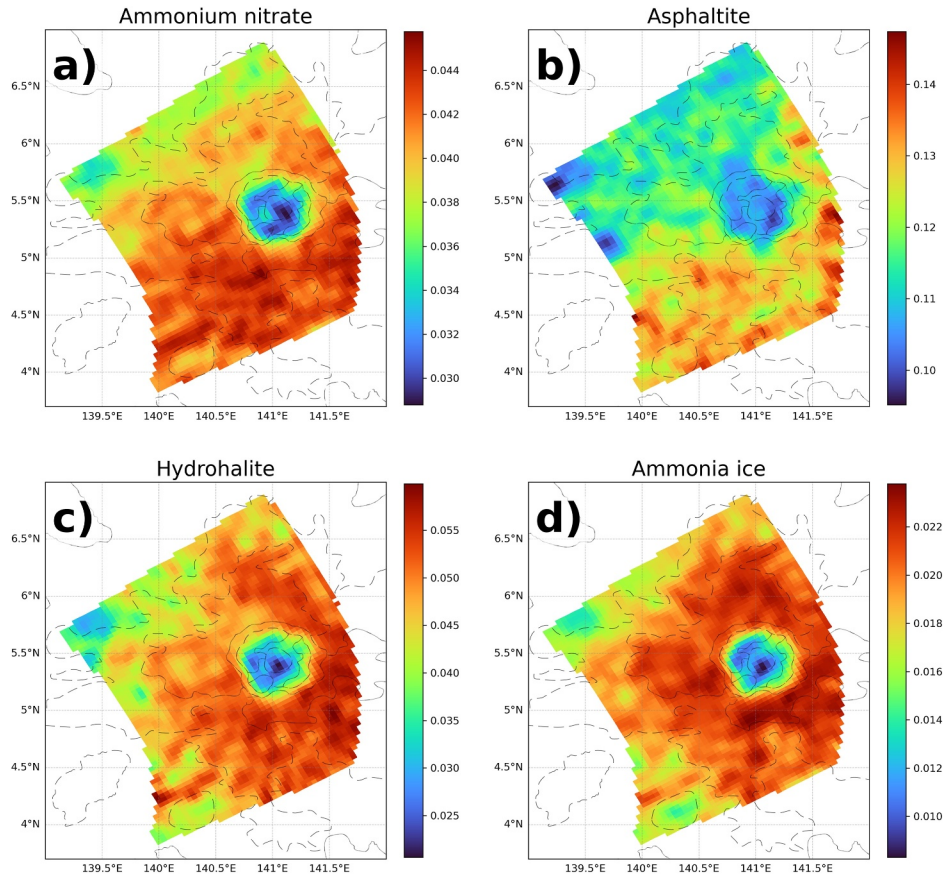

Figure 11. Distribution of ammonium nitrate (a), asphaltite (b), hydrohalite (c), and ammonia ice (d) in the Antum Crater Region using the Fully Constrained Least Squares method. The scalar coefficients associated with these compounds suggest a smaller contribution of contaminants in the crater floor, consistent with the spectral indices shown in Figure 6. To facilitate comparison, the geological units mapped in Figure 3 are overlaid with dashed grey contours.

We then extended the FCLS method to all pixels in order to map the distribution of contaminants in the ACR. These maps show the distinctive distribution of specific endmembers, such as ammonium nitrate, asphaltite, hydrohalite, and ammonia ice (Figures 11a–11d). The application of linear spectral unmixing to NIMS data

Table 2
Scalar Coefficients of the Linear Combination Estimated With the FCLS Algorithm for Each Regions of Interest

Endmember	CF1	CF2	DE1	DE2	OR1	OR2
Water ice 70-μm	10.2 ± 1.4	9.7 ± 1.3	6.4 ± 1.4	6.1 ± 1.5	9.1 ± 1.6	8.5 ± 1.6
Water ice 1,360-μm	8.2 ± 0.4	7.9 ± 0.4	5.2 ± 0.3	5.0 ± 0.3	7.0 ± 0.5	6.4 ± 0.6
Burkeite	2.6 ± 2.9	2.6 ± 2.9	3.1 ± 2.9	2.5 ± 2.7	2.8 ± 2.7	3.5 ± 2.8
Ammonia ice	1.1 ± 2.4	1.1 ± 2.4	2.1 ± 2.5	2.2 ± 2.7	1.5 ± 2.6	1.8 ± 2.6
Asphaltite	7.4 ± 0.8	7.5 ± 0.6	9.3 ± 0.7	8.6 ± 0.8	7.8 ± 0.7	8.7 ± 0.7
Ammonium nitrate	4.6 ± 2.4	4.5 ± 2.5	5.0 ± 2.8	4.4 ± 2.7	4.8 ± 2.7	5.7 ± 2.6
Hydrohalite	2.1 ± 0.5	2.1 ± 0.5	2.2 ± 0.6	1.8 ± 0.6	2.7 ± 0.6	3.5 ± 0.5
Bloedite	6.1 ± 2.1	6.0 ± 2.2	4.2 ± 2.0	3.8 ± 2.0	3.4 ± 2.2	5.9 ± 2.4
Black	53.4 ± 11.1	54.0 ± 11.3	55.0 ± 11.1	58.9 ± 11.5	54.6 ± 11.9	50.6 ± 12.0
White	0.3 ± 11.0	0.3 ± 11.3	0.4 ± 11.0	0.4 ± 11.6	0.3 ± 11.4	0.3 ± 11.8

Table 3
Estimated Scalar Coefficients With the MCMC Algorithm for Each Regions of Interest

Endmember	CF1	CF2	DE1	DE2	OR1	OR2
Water ice 70-μm	9.5 ± 1.5	8.9 ± 1.6	4.8 ± 1.6	3.8 ± 1.4	7.9 ± 1.8	8.0 ± 1.5
Water ice 1,360-μm	7.0 ± 0.7	6.9 ± 0.7	5.2 ± 0.5	5.4 ± 0.5	6.3 ± 0.6	6.0 ± 0.6
Burkeite	4.7 ± 2.8	4.8 ± 2.8	5.3 ± 2.9	4.6 ± 2.7	4.8 ± 2.7	6.0 ± 2.6
Ammonia ice	1.1 ± 2.7	2.1 ± 2.8	2.2 ± 3.2	2.2 ± 2.9	1.5 ± 2.7	1.8 ± 2.8
Asphaltite	11.0 ± 1.0	10.8 ± 1.1	12.4 ± 1.2	11.2 ± 1.1	10.9 ± 1.1	12.6 ± 1.3
Ammonium nitrate	3.3 ± 2.3	3.3 ± 2.8	4.3 ± 2.8	4.1 ± 2.8	3.7 ± 2.7	4.3 ± 2.8
Hydrohalite	2.9 ± 0.7	2.9 ± 0.7	5.8 ± 0.6	5.2 ± 0.5	3.6 ± 0.7	4.9 ± 0.7
Bloedite	0.2 ± 2.0	0.2 ± 2.0	0.0 ± 2.0	0.0 ± 2.0	0.0 ± 2.0	0.0 ± 2.0
Black	60.4 ± 12.1	61.2 ± 12.3	59.9 ± 12.2	63.5 ± 12.5	61.3 ± 12.0	56.4 ± 12.0
White	0.0 ± 12.0	0.0 ± 12.0	0.0 ± 12.0	0.0 ± 12.0	0.0 ± 12.0	0.0 ± 12.0

presents several challenges, such as the difficulty of identifying carbon dioxide, the inability to detect exogenous compounds above the noise level, and the unreasonably large contribution of asphaltite.

3.3. Potential Primitive Impactor Remnant?

Hibbitts (2023) suggested that some DRCs on Ganymede, including Antum, might display a composition consistent with a mixture of water ice, hydrated non-ice material endemic to Ganymede, and a less hydrated non-ice component characterized by a 3-μm absorption band. The spectral characteristics of this secondary non-ice component suggest that it could be hydrated carbonaceous material, possibly linked to a primitive impactor or the excavation of ancient non-ice material from Ganymede.

To test this hypothesis, we subtracted the previously modeled spectra for each ROI from the original NIMS data and applied linear spectral unmixing in the 1.00–4.75 μm range to the residual spectra. We considered a small spectral library of carbonaceous chondrite meteorites (Table 4), which are representative of the potential contribution of a C-type asteroid.

Our modeling identifies the Alais CI1 meteorite as the best endmember; however, absorption bands at 1.25, 1.50, and 2 μm in the residual spectra suggest that hydrates are still present. Adding the Alais meteorite endmember to the previous model, along with water ice and salts, and "black" and "white" synthetic spectra (organics are excluded to avoid overlap with the meteorite's spectral signature beyond 3 μm), does not significantly improve the results, except for a decrease in the relative weight of the "black" spectrum, with its scalar coefficient in the dark ejecta settling around 20%. This may be due to the relatively flat spectrum of the Alais meteorite (except for the 3-μm band) or it could indicate the presence of exogenous carbonaceous material.

Table 4
Carbonaceous Chondrites Considered in This Study to Account for the Potential Contribution of Impactor Material in the Antum Spectra

Name	Type	RELAB spectrum ID
Orgueil	CI1	bmr1mt191
Alais	CI1	bir1mt264
Murchison	CM2	bir1mb064d1
Tagish Lake	C2-ung	bir1mt025b
MET01070	CM1	bir1mt218

Note. The first column lists the meteorite names, the second column identifies their types, and the third column provides the corresponding RELAB spectrum ID (https://pds-speclib.rsl.wustl.edu/).

In summary, linear spectral unmixing cannot rule out the presence of residual impactor material, but it cannot quantify its contribution either. However, an upper limit for the contribution of carbonaceous exogenous material in this area may be set at around 20%.

3.4. Non-Linear Spectral Unmixing

To address the limitations of linear spectral unmixing, we employed a non-linear spectral unmixing approach based on Hapke's theory (see Text S1 in Supporting Information S1 for details). To ensure consistency between the linear and non-linear methods, we utilized the same optimal spectral endmembers previously identified through FCLS and MCMC, excluding ammonia ice, which was found to be a negligible contributor in the linear model. Burkeite, on the other hand, is included because it exhibits negligible abundance with the FCLS method but not with MCMC (Tables 2 and 3).

Table 5
Estimated Abundances in Regions of Interest Covering the Antum Crater Region Using Non-Linear Hapke Modeling

Endmember	CF1	CF2	DE1	DE2	OR1	OR2
Water ice	40.9	37.6	20.9	25.3	33.3	35.6
Carbon dioxide	2.6	1.9	1.1	1.8	1.1	1.2
Burkeite	0.7	0.5	1.8	0.6	2.4	1.9
Asphaltite	0.4	0.3	4.5	0.3	0.6	0.3
Ammonium nitrate	7.1	6.1	6.1	6.8	7.3	8.6
Hydrohalite	25.5	22.9	32.0	31.5	25.8	36.4
Bloedite	0.8	0.8	0.4	1.1	1.2	0.4
Hydrated sulfuric acid	0.8	0.6	2.3	1.5	1.2	1.2
Black	20.8	29.1	29.9	26.2	27.2	13.0
White	0.8	0.2	0.3	0.6	0.3	0.3

Note. The associated uncertainties, derived from the MCMC corner plots, are detailed in Table S3 of Supporting Information S1.

Additionally, we incorporated carbon dioxide (CO_2) and hydrated sulfuric acid ($H_2SO_4{\cdot}8H_2O$), whose refractive indices are available in the literature or can be retrieved.

The non-linear spectral unmixing approach corroborates the distribution of water ice observed via spectral indices and linear unmixing methods, with the highest abundances located in the crater floor region (Table 5). Specifically, CF1 exhibits higher water ice abundance compared to CF2. Dark ejecta exhibit the lowest water ice abundance, whereas areas outside the Antum crater show water ice levels comparable to those expected at equatorial latitudes on Ganymede's trailing hemisphere (King & Fletcher, 2022).

Among salts, hydrohalite exhibits the highest abundance, which is consistent with recent observations of local-scale regions of Ganymede (Tosi, Mura, et al., 2024), supporting the hypothesis of subsurface liquid extrusion following crater formation. The detection of ammonium nitrate suggests the possible presence of ammoniated salts, although further analysis is needed to confirm this hypothesis. Unlike the linear unmixing approach, non-linear unmixing identifies carbon dioxide, as anticipated by spectral index analysis (Figures 5d and 7c). The resulting abundances are similar throughout the different ROIs, confirming the lack of clear evidence for correlation with the different terrain types (Hibbitts et al., 2003). Hydrated sulfuric acid is relevant in dark ejecta and distant regions, suggesting that the terrain where Antum formed was exposed to exogenic influences long before the impact event. The abundances of hydrated sulfuric acid in OR1 and OR2 are comparable to those reported in recent studies for similar latitudes in Ganymede's trailing hemisphere (King & Fletcher, 2022). Furthermore, the abundances of asphaltite, representing organic compounds, are lower compared to those obtained with the linear approach.

The estimated water ice grain sizes (Table 6) reveal notable differences between the crater floor and surrounding regions. In CF1 and CF2, the grain sizes are larger than those in DE1 and DE2, which aligns with expected distributions. Water ice grain sizes in CF1 and CF2 are approximately 2.5 mm, while in dark ejecta, the sizes are slightly smaller (~1.7 mm). Other regions exhibit water ice grain sizes consistent with those expected for equatorial latitudes on Ganymede (~2.2 mm) (King & Fletcher, 2022; Stephan et al., 2020).

In all ROIs, the grain sizes of CO_2 and hydrated sulfuric acid are much smaller than those of other endmembers (Table 6). The small grain size of CO_2 may be attributed to the optical constants used in the simulations. Specifically, the refractive index for CO_2 ice (Soderblom et al., 2009) does not accurately represent its complexed form on Ganymede, leading the model to minimize the grain size to best fit the observed 4.25-μm absorption band. This effect is tied to the single-scattering albedo model for CO_2 ice, which reduces the characteristic double minima of the CO_2 band at 4.27 μm for smaller grain sizes, thus aligning more closely with the observed 4.25-μm band. A smaller grain size, on the order of tens of microns, corresponds to a narrower absorption bandwidth, which matches the observed spectral features. In contrast, larger grain sizes lead to a broader absorption bandwidth and stronger double minima, resulting in significant deviation from the observed data (Figures 4 and 6). Hydrated sulfuric acid exhibits comparable behavior, likely reflecting the slow formation rate of exogenous compounds at equatorial latitudes (Ding et al., 2013). In all ROIs, hydrohalite exhibits comparable grain sizes. Bloedite displays millimeter-scale grain sizes, except in OR1. Further investigation of the remaining compounds is necessary, as their optical constants were modeled rather than directly measured (Shkuratov et al., 1999).

Macroscopic surface roughness, modeled via Hapke's shadowing function (Hapke, 1984), in principle could be linked to topographic relief. However, the large uncertainties associated with these values, stemming from less informative priors, prevent any conclusions regarding topographic variability.

Table 6
Grain Sizes (in μm) for Each Endmember as a Result of Non-Linear Spectral Unmixing

Endmember	CF1	CF2	DE1	DE2	OR1	OR2
Water ice	2,587	2,574	1,773	1,710	2,193	2,190
Carbon dioxide	28	20	21	17	17	22
Burkeite	1,785	1,801	2,195	1,299	1,644	1,850
Ammonium nitrate	1,636	1,896	2,475	753	1,891	1,636
Hydrohalite	292	372	288	188	343	353
Bloedite	1,075	1,036	1,395	1,374	471	1,140
Hydrated sulfuric acid	62	51	56	50	54	54

Note. Uncertainties are derived from corner plots and are provided in Table S4 of Supporting Information S1.

4. Impact Modeling

We conducted a series of numerical simulations to model the bulk characteristics of the Antum crater on Ganymede. These simulations were performed using the iSALE-2D shock physics code (Dellen version), originally developed by Amsden et al. (1980) and subsequently enhanced by several authors to simulate collisional processes (e.g., Collins, 2014; Collins et al., 2004; Ivanov et al., 1997; Melosh et al., 1992; Wünnemann et al., 2006; Wünnemann & Ivanov, 2003). iSALE has been extensively tested against laboratory experiments at both low and high strain rates (Wünnemann et al., 2006) and validated through comparisons with other hydrocodes (Luther et al., 2022; Pierazzo et al., 2008; Stickle et al., 2020).

We ran multiple simulations to best reproduce the 25-km Antum impact structure, varying the projectile radius, impact velocity, and target surface properties. Detailed descriptions of the iSALE-2D code and model setup are provided in the Supporting Information S1, Text S2.

The impactor was assumed to have a bulk density of water ice (910 kg/m^3). Based on impactor flux data within the Jovian system, an average impact velocity of 20 km/s was adopted for Ganymede (McKinnon & Schenk, 1995; Nesvorný et al., 2023; Zahnle, 1992, 2003). Additionally, two lower impact velocities were considered—15 km/s, commonly used in previous numerical studies (e.g., Bjonnes et al., 2022; Bray et al., 2008; Silber & Johnson, 2017), and 10 km/s, to account for a potential slower impactor hitting Ganymede's trailing hemisphere, as suggested by Hibbitts (2023) for DRCs.

The best-fit results were obtained with projectile radii of 600, 700, and 750 m for impact velocities of 20, 15, and 10 km/s, respectively, assuming a thermal gradient of 10 K/km. We also evaluated the effects of lower and higher thermal gradients, consistent with the estimated range of surface heat flux from the formation of Ganymede's most ancient terrains (60–80 mW/m^2) to present-day values (~3–4 mW/m^2) (Bjonnes et al., 2022).

Figure 12 presents a series of snapshots comparing crater formation at three different impact velocities. Figures 12a–12c show the initial configuration at 0 s. The transient cavity reaches its maximum volume at approximately 42, 43, and 37 s after impact for the 20, 15, and 10 km/s cases, respectively (Figures 12d–12f). These time steps mark the end of the excavation phase. Following this, material ejected on ballistic trajectories is deposited around the cavity, while the central part of the crater begins to uplift. The central uplift reaches its maximum height in Figures 12g–12i, with the smallest elevation occurring in the 10 km/s case, and it then collapses. Oscillations of the crater floor are evident from the deformation of the overlaid Lagrangian mesh.

The final crater morphologies are shown in Figures 12j–12l. All three craters exhibit a subdued central peak and a rim elevated approximately 0.5 km above the pre-impact surface for the 20 and 15 km/s cases. The rim is significantly lower in the 10 km/s scenario.

As summarized in Table 7, the final crater diameters are approximately 25 km across all tests we carried out with different combinations of projectile size and impact velocity. The crater depth reaches about 2.6 km at 20 km/s and 15 km/s, decreasing to ~2.0 km at 10 km/s, yielding a depth-to-diameter ratio of ~0.08–0.10. The simulation with 10 km/s also shows a modest region of elevated post-impact temperatures near the crater center, consistent with findings by Bjonnes et al. (2022).

To account for differences in impact velocity and kinetic energy, we compared these cases using dimensionless scaling parameters. Following established π-group scaling approaches (see Supporting Information S1, Text S2), we analyzed the relationship between crater dimensions and impact conditions using parameters that capture the effects of gravity and material properties. A power-law fit to our data yields scaling constants that differ from previous studies, likely due to variations in modeling approaches and thermal assumptions. Full definitions, equations, and fitting details are provided in the Supporting Information S1, Text S2.

A more pronounced effect on cavity formation and final crater morphology was observed when varying the thermal gradient, as shown in Figure 13. Holding impact velocity (20 km/s) and projectile radius (600 m) constant, we tested models with thermal gradients of 5, 10, and 15 K/km. At the end of the excavation phase (Figures 13d–13f), the transient cavity is larger for higher thermal gradients. The uplift of the crater floor is also strongly influenced by this parameter. In the 5 and 10 K/km models (Figures 13g and 13h), the central peak fails to reach the surface before collapsing. In contrast, the 15 K/km model (Figure 13i) shows a substantially larger uplift, reaching approximately 1.5 km above the pre-impact surface.

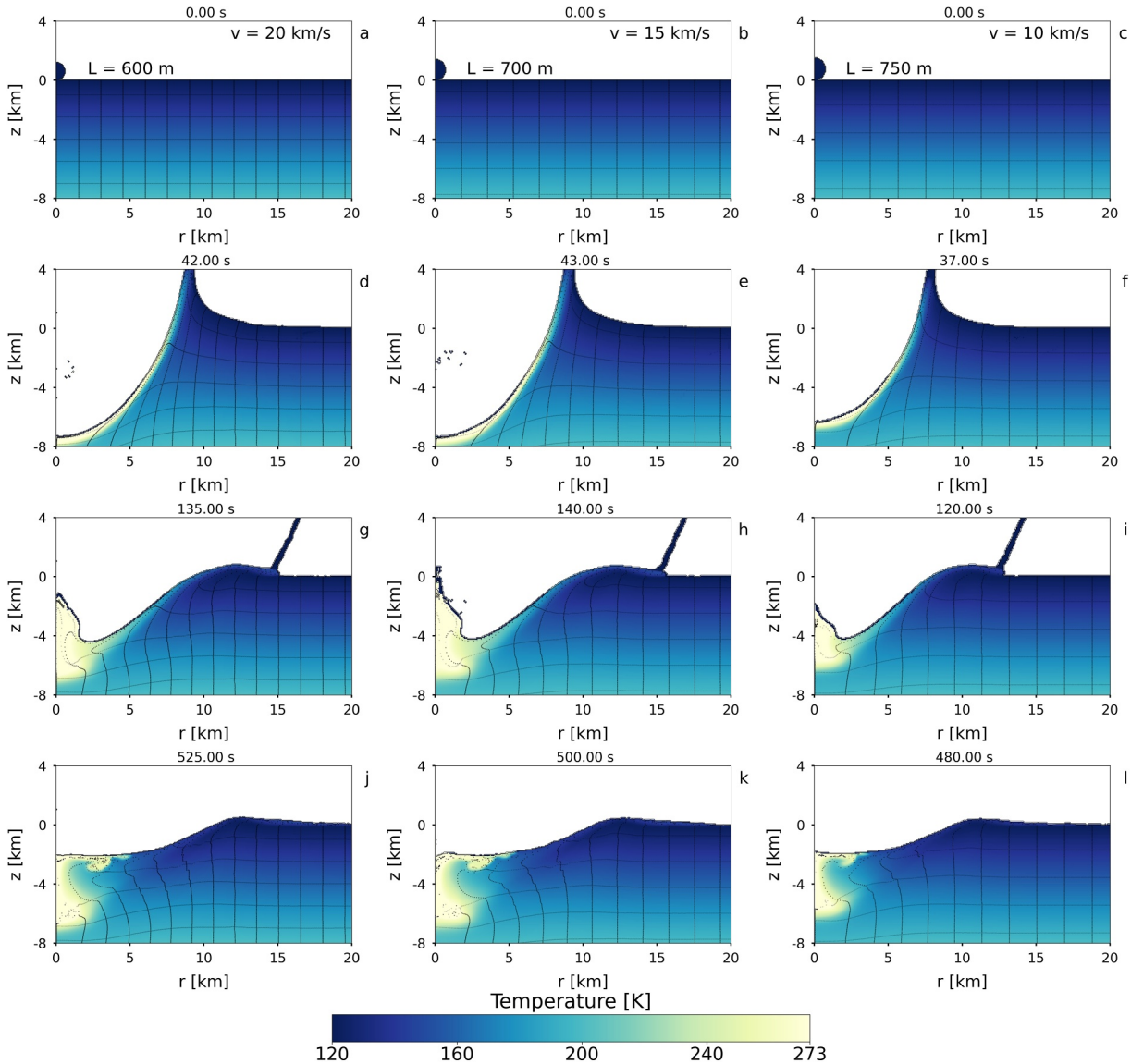

Figure 12. Snapshots from the Antum crater simulations, assuming impact velocities of 20 km/s (left column), 15 km/s (center column), and 10 km/s (right column). The corresponding projectile radii are 600, 700, and 750 m. Each row represents a distinct stage of the impact process: (a–c) initial contact; (d–f) transient cavity formation; (g–i) ejecta emplacement and peak uplift of the crater floor; and (j–l) final crater morphology. All panels display the temperature distribution during cavity formation. A Lagrangian mesh is superimposed on the models.

Table 7
Summary of Best-Fit Simulation Results for Varying Impact Velocities

Symbol	Definition	Best fit values		
		20 km/s	15 km/s	10 km/s
R_p	Projectile radius [m]	600	700	750
D_c	Crater diameter [km]	25.20 ± 0.95	25.34 ± 0.97	24.60 ± 1.08
d_c	Crater depth [km]	2.61 ± 0.12	2.58 ± 0.14	1.95 ± 0.15
d/D	Depth-to-diameter ratio	0.10 ± 0.01	0.10 ± 0.01	0.08 ± 0.01
H_p	Central peak height [km]	0.07 ± 0.12	0.00 ± 0.14	0.07 ± 0.15

Note. Projectile radii range from 600 to 750 m for impact velocities decreasing from 20 to 10 km/s, respectively. All models assume a thermal gradient of 10 K/km.

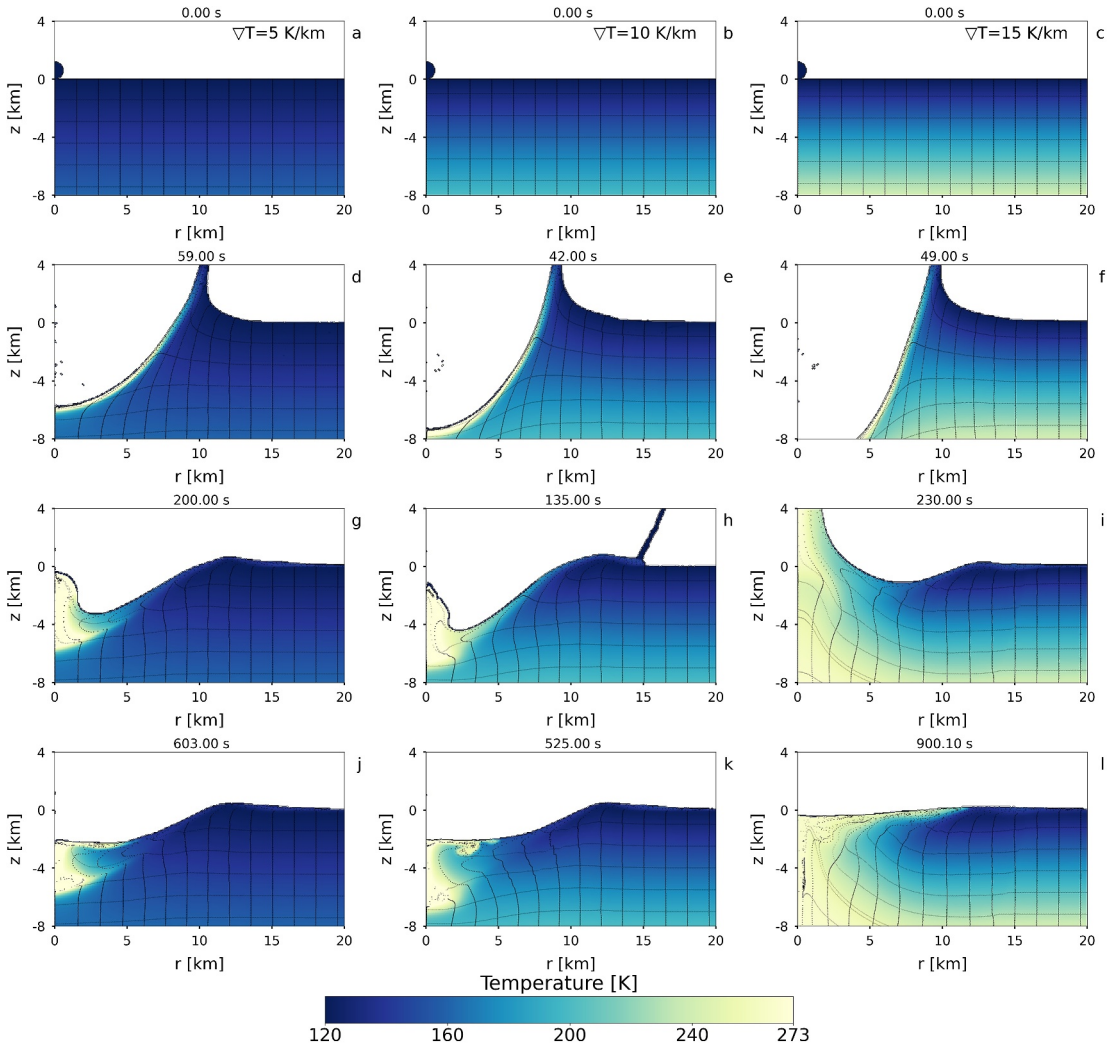

Figure 13. Snapshots from the Antum crater simulation using an impact velocity of 20 km/s and a projectile radius of 600 m illustrate the influence of the thermal gradient on the impact process. The three columns correspond to thermal gradients of 5 K/km, 10 K/km, and 15 K/km, respectively. Each row shows the same impact stage: (a–c) initial contact; (d–f) transient cavity formation; (g–i) ejecta emplacement and initial uplift of the crater floor; and (j–l) final crater morphology. All panels display the temperature distribution during cavity formation. A Lagrangian mesh is superimposed on the models.

The final crater morphologies (Figures 13j–13l), shown after several hundred seconds and without accounting for post-impact viscous relaxation, reveal no fully developed central peak in any case. Similar results were reported by Bjonnes et al. (2022) for 25 km-scale craters, suggesting that this crater size lies near the morphological transition where peak formation becomes suppressed. The absence of a prominent central peak may be explained by the fact that the Antum crater lies near the so-called "Transition II" regime, where an inverse trend in depth-to-diameter ratio occurs with increasing crater size (Bjonnes et al., 2022; Schenk, 2002).

As also noted by Bjonnes et al. (2022), the final structure formed in the model with a 15 K/km gradient is notably shallower than those with lower gradients. The depth-to-diameter ratio trends, summarized in Figure 14, show a clear inverse correlation with thermal gradient: crater depth decreases as the thermal gradient increases (from blue to red in Figure 14).

We next investigated the influence of target layering on the final crater morphology. Figure 15 shows four simulations with varying thicknesses of an upper porous ice layer (yellow), overlying a non-porous substrate (pale blue). To isolate the effects of layering, all other parameters were held constant: projectile radius of 600 m, impact

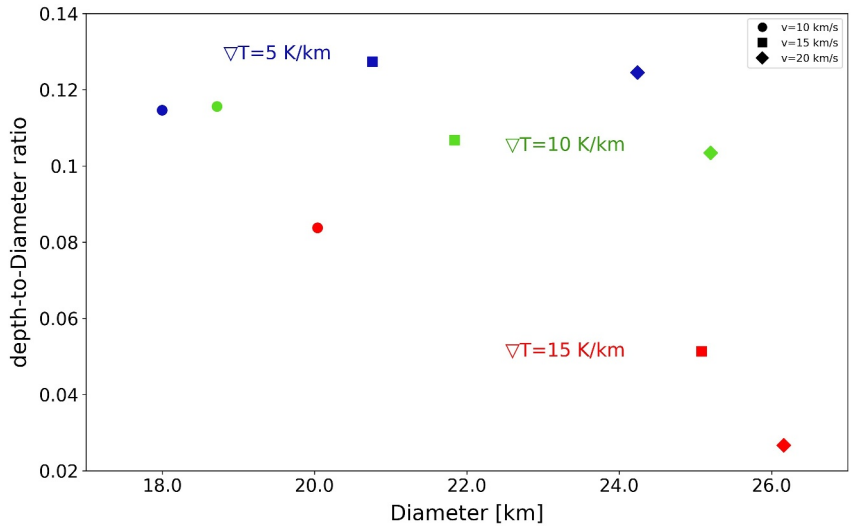

Figure 14. Depth-to-diameter ratios as a function of crater diameter for different impact velocities. Colors indicate the thermal gradients used in the simulations: blue for 5 K/km, green for 10 K/km, and red for 15 K/km.

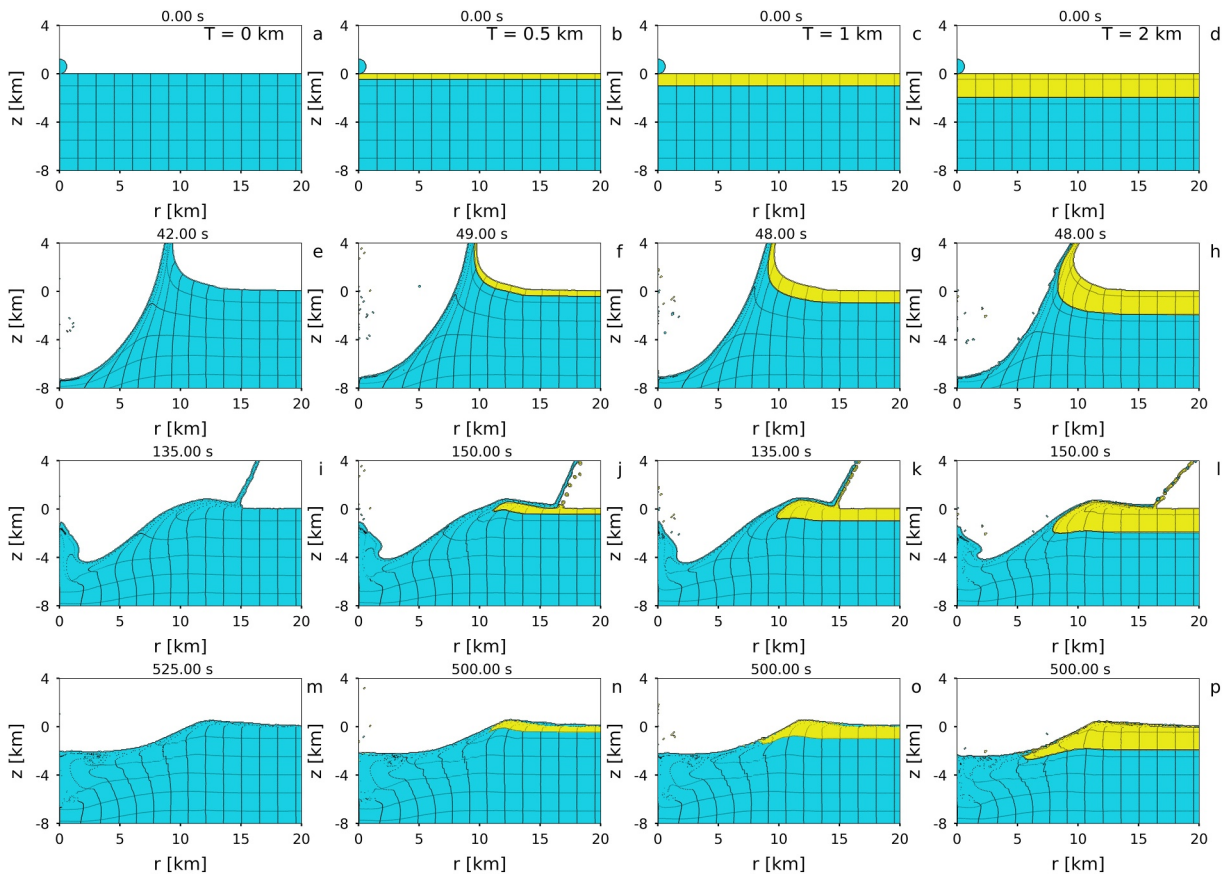

Figure 15. Snapshots of crater formation under varying upper porous layer thicknesses (0–2 km), with fixed impact velocity (20 km/s), projectile radius (600 m), and thermal gradient (10 K/km). Yellow indicates porous ice (upper layer); pale blue indicates non-porous ice (lower layer). Each column represents a different layer thickness. Each row corresponds to a stage in the cratering process: (a–d) initial contact; (e–h) transient cavity formation; (i–l) ejecta deposition and maximum central uplift; and (m–p) final crater morphology. A Lagrangian grid is overlaid on the models.

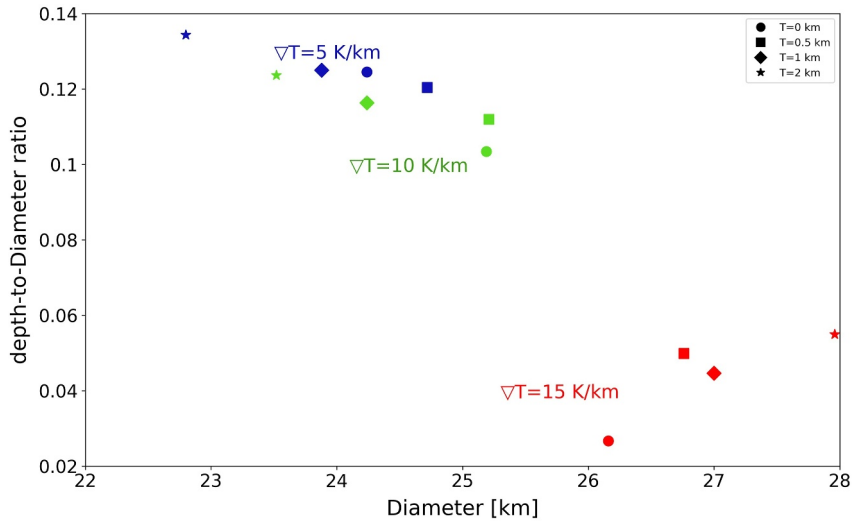

Figure 16. Depth-to-diameter ratios as a function of crater diameter for layered target models. Colors indicate the thermal gradients used: blue for 5 K/km, green for 10 K/km, and red for 15 K/km.

velocity of 20 km/s, and a thermal gradient of 10 K/km. These settings correspond to the best-fit conditions for the homogeneous case (0 km porous layer) shown in the first column of Figure 15.

Crater evolution remains generally consistent across the four cases, with the most noticeable differences arising in the ejecta distribution. For thinner porous layers (0.5 and 1 km; Figures 15j and 15k), the non-porous basement contributes significantly to the ejecta, which blankets the porous surface layer. In contrast, thicker porous layers result in a two-component ejecta curtain: non-porous material becomes increasingly confined to the inner crater and rim areas (Figure 15p), while the porous ice dominates the ejecta beyond the rim.

The presence of an upper porous layer produces at most a ∼10% variation in the final crater diameter. The depth-to-diameter ratio changes by approximately two percentage points and follows the same general trend observed with varying thermal gradients (Figure 16): deeper craters form under lower thermal gradients, while higher gradients result in shallower final structures.

Finally, we examined the role of surface cohesion in crater development. Figure 17 compares the final crater topographies for different cohesion values. In stronger targets (cohesion Y_d = 500 kPa, see Supporting Information S1, Text S2), craters are deeper and exhibit a bowl-shaped morphology, with no central peak formation except in the case of high thermal gradients (red dashed line in Figure 17).

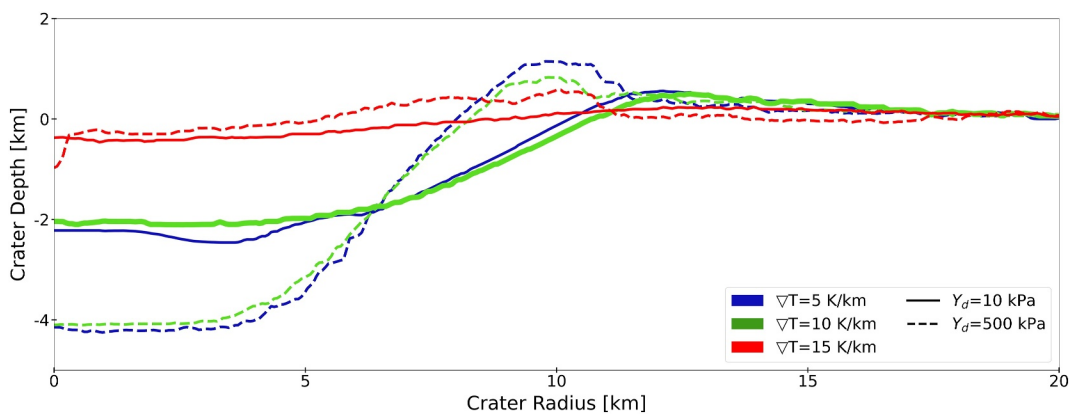

Figure 17. Comparison of final crater topographies for simulations with different thermal gradients and surface cohesion values. All cases used a projectile with a radius of 600 m and an impact velocity of 20 km/s.

5. Discussion

The study of Antum crater on Ganymede unveils a multifaceted narrative of impact dynamics, compositional evolution, and geological interplay, rooted in the synthesis of high-resolution spectral data, numerical simulations, and stratigraphic mapping. At its core, the crater's formation—modeled through iSALE-2D simulations as the result of a hypervelocity impact by a 600–750 m water ice projectile traveling at 20–10 km/s—highlights the unique rheology of Ganymede's ice-dominated crust. The presence of a porous upper layer (0–2 km thick) critically controls crater morphology and ejecta characteristics: thinner layers allow excavation of denser, non-porous substrates, while thicker layers produce ejecta dominated by disaggregated porous ice. The shallow morphology (depth/diameter ∼0.10) and the absence of a prominent central peak reflect the "Transition II" between complex and anomalous craters (Schenk, 2002) in the case of low-cohesion targets like Ganymede, likely comprising a mixture of water ice and unconsolidated regolith. This porous structure, inferred from both simulations and spectral data, explains the finer grains observed in the dark ejecta, which originated from the mechanical breakdown of the friable upper layer during impact.

Geologic mapping reveals an asymmetric ejecta distribution, with dark-rayed material extending northwestward, indicative of a southeast-to-northwest impact trajectory. This directional bias aligns with spectral detections of non-ice contaminants in specific regions, materials likely scavenged from Ganymede's pre-impact surface and redistributed during the ballistic emplacement phase. The porous layer's role as a reservoir for volatiles is evident in the retention of complexed CO_2 and hydrated salts within the ejecta, shielded from sublimation by the overlying regolith until excavated. The contrast between the crater floor's pristine, coarse-grained ice (1–3 mm) and the ejecta's fine-grained, contaminant-rich material underscores the crater's role as a geological window: impacts excavate shielded subsurface volatiles while scattering and mixing surface contaminants, creating a compositional dichotomy that encodes both the target's internal structure and its surface history.

The spectral data from Galileo/NIMS provided detailed insights into the post-impact processes on Antum's floor and ejecta. The crater floor's deeper 2-μm water ice absorption bands and minimal contaminants signal the exposure of ancient, radiolytically shielded ice, preserved by Ganymede's intrinsic magnetic field. In contrast, the dark ejecta's subdued ice bands and hydrated salt signatures—coupled with a 2-μm band shift to shorter wavelengths—imply contamination by pre-existing surface materials, including hydrated carbonaceous compounds and endogenous salts. These salts, such as hydrohalite ($NaCl{\cdot}2H_2O$), may originate from brines mobilized by impact-induced heating of the porous layer, suggesting transient aqueous activity in the crater's aftermath. The detection of complexed CO_2 and hydrated sulfuric acid in distal regions further points to a volatile-rich subsurface environment, where impacts act as catalysts for both exposing and altering chemical inventories. In ejecta, the spectral similarity of ammonium nitrate introduces intriguing questions about the presence of ammoniated compounds on Ganymede and their source. Residual measured-minus-modeled spectra do not rule out the presence of carbonaceous material, which could represent a remnant of the impactor body. However, an alternative possibility is that this material was already present in the dark terrain, concentrated in the uppermost surface lag due to prolonged micrometeoritic bombardment (Hibbitts, 2023; Stephan et al., 2025), particularly given that Antum is located within the dark, ancient Marius Regio. The persistence of water absorption bands suggests the continued presence of hydrated phases, implying an upper limit of ∼20% for any exogenous, carbonaceous contribution.

Geologically, Antum's formation is superimposed on a terrain shaped by tectonic resurfacing and prior impacts. The Tiamat Sulcus, with its grooved (sT) and smoother peripheral units (sT1), represents a pre-existing tectonic framework that influenced ejecta deposition patterns. The dark ejecta blanket obscures ancient concentric rings and palimpsest-like features, suggesting that Antum's event reset the regional geological record, while interactions with the sulcus's topography hint at syn-impact stress redistribution or post-impact readjustment. The discontinuous bright patches (rt3 facies) within the ejecta may represent localized frost deposition or volatile retention, offering clues to microenvironments where transient sublimation-condensation cycles persist. This dynamic resurfacing narrative is further complicated by the detection of hydrated sulfuric acid ($H_2SO_4{\cdot}8H_2O$) in distal regions, a compound typically linked to exogenic radiolysis of sulfur implanted by Jovian magnetospheric particles. Its presence in ejecta implies that Antum's impact occurred on terrain already processed by Ganymede's radiation environment, with the event itself redistributing and possibly modifying these exogenous compounds.

The broader implications of this study extend beyond Ganymede, offering a template for understanding impact processes on ocean worlds. The composition and physical characteristics of the ejecta are consistent with a two-

layer structure, in which the upper layer is porous, influencing the crater morphology and the distribution of the ejected material. The excavation of subsurface ice and the mobilization of brines at Antum mirror hypothesized processes on Europa and Enceladus, where impacts could breach icy shells to release subsurface materials. The dark-rayed ejecta's compositional signature parallels impact features on other icy bodies, suggesting universal mechanisms of impact-driven surface alteration. Furthermore, the detection of chloride and potentially ammonium salts in ejecta raises astrobiological questions: could impact-induced heating create transient habitable niches by mobilizing brines, or facilitate redox chemistry through the introduction of reactive nitrogen species? While speculative, these are hypotheses for the JUICE mission to test, and underscore the need to view impacts not merely as destructive events but as potential enablers of chemical complexity.

Methodologically, the study's integration of spectral unmixing with impact modeling exemplifies the power of interdisciplinary approaches. The FCLS and MCMC linear unmixing models, while effective in identifying hydrated salts and organics, struggle to resolve complexed CO_2—a limitation overcome by Hapke's radiative transfer model, which accounts for intimate mixing of ices and contaminants. This methodological synergy not only refined the detection of CO_2 but also highlighted the pitfalls of assuming linear mixing in icy regoliths, where scattering effects dominate. Similarly, the numerical simulations' reliance on π-group scaling laws revealed discrepancies with prior Ganymede models, emphasizing the need to recalibrate scaling parameters for icy targets with variable porosity and thermal gradients.

The scientific case of the Antum crater epitomizes the dual nature of impacts on icy moons: destructive yet revelatory, chaotic yet systematic. By excavating pristine subsurface ice, redistributing surface contaminants, and potentially mobilizing brines, Antum's formation encapsulates the dynamic processes that shape icy world surfaces. This study offers a comprehensive understanding of how both the physical and chemical properties of Ganymede's surface were modified during and after the impact event that formed the Antum crater. Our approach connects the observable compositional diversity—such as the differences in water ice and the presence of salts and hydrated compounds—to the impact processes and their aftermath. By synthesizing geological, spectral, and modeling data, this work underscores the complexity of the processes that shaped Ganymede's surface and its geological history, contributing to a deeper understanding of the icy moons of the outer Solar System.

6. Future Implications for JUICE

The exploration of Antum Crater by JUICE's suite of remote sensing instruments—JANUS, MAJIS, UVS, RIME, GALA, and SWI—will unlock a transformative understanding of this complex impact feature, revealing the interplay between surface morphology, subsurface structure, and chemical evolution on Ganymede. Each instrument brings unique capabilities, but their true power lies in their synergies, enabling a multi-layered, interdisciplinary approach to studying Antum.

JANUS, the high-resolution optical camera (Palumbo et al., 2025), will map the crater's rim, walls, floor, and asymmetric ejecta blanket at resolutions better than 10 m/pixel, providing the foundational context for all other observations. Further ROIs, such as bright patches within the ejecta, could be revealed, which may represent localized frost deposition or volatile retention. These high-resolution images will also allow deriving Digital Elevation Models (DEMs) essential for correcting surface clutter in RIME's radar data, ensuring accurate subsurface profiling. By overlapping its spectral range with MAJIS's hyperspectral capabilities, JANUS will enable the identification of compositional units at finer spatial scales, linking surface materials to their geological context. For example, the contrast between the pristine ice on the crater floor and the contaminant-rich ejecta can be mapped in detail, revealing how it impacts redistribute and mix materials on Ganymede's surface.

MAJIS, the visible and infrared imaging spectrometer (Poulet et al., 2024), will decode the compositional complexity of Antum's floor and ejecta, detecting hydrated salts (e.g., hydrohalite, bloedite), complexed CO_2, sulfuric acid hydrate, and possibly ammoniated salts. Its hyperspectral data will complement JANUS's imagery by mapping these compounds at sub-100 m scales, particularly in regions where dark ejecta's spectral signatures correlate with fractures or bright patches observed by JANUS. MAJIS's potential detection of ammoniated salts could raise astrobiological questions: are these compounds a relic of impact-driven brine chemistry, or do they hint at endogenous nitrogen cycling? To answer this question, MAJIS will work in tandem with UVS, the JUICE Ultraviolet Spectrograph nearly twin of its counterpart on Europa Clipper (Retherford et al., 2024), which can detect radiolytically altered compounds like H_2SO_4 and O_3. UVS's far-UV spectra could help map the distribution of sulfur and ammoniated species across the crater. If Antum's floor shows less H_2SO_4 than ejecta, it implies the

impact exposed ancient, radiolytically shielded ice—supporting the hypothesis that Ganymede's magnetic field preserves subsurface chemistry. UVS's observations will also complement PEP's neutral gas measurements (Föhn et al., 2021), revealing whether Antum's ejecta contributes to Ganymede's tenuous atmosphere.

RIME, the radar instrument (Bruzzone & Croci, 2019), will penetrate Ganymede's ice shell to depths of a few km, providing a unique view of Antum's subsurface structure. Its radargrams will reveal the stratigraphy beneath the crater, including layers of porous ice, fractured regions, or brine pockets mobilized by the impact. Notably, Antum's location on the anti-Jovian side of Ganymede at low latitudes favors shielding from Jupiter's intense radio noise, improving the signal-to-noise ratio for RIME observations. However, RIME's success in Antum's rough terrain also depends on high-resolution topographic data from JANUS and GALA to correct for surface clutter and isolate subsurface signals. If MAJIS detects surface salts linked to brines, RIME could target those regions to seek dielectric anomalies, potentially confirming Antum's impact as a conduit for subsurface-ocean material. This synergy between surface composition (MAJIS) and subsurface structure (RIME) will test the hypothesis that impacts mobilize Ganymede's subsurface ocean, creating transient habitable niches.

GALA, the laser altimeter (Hussmann et al., 2025), will provide precise topographic measurements of Antum Crater and its surroundings, generating high-resolution DEMs that enhance the interpretation of JANUS's images and RIME's radar data. By studying the relationship between Antum's ejecta and pre-existing tectonic features such as Tiamat Sulcus, GALA will clarify how the impact interacted with Ganymede's crust. Its global mapping of Ganymede will also place Antum in a broader geological context, aiding in the understanding of regional resurfacing processes and the moon's thermal evolution. The resolution of GALA's terrain models, influenced by profile spacing, ranges from a few hundred meters at the poles to several kilometers at the equator, affecting the DEM detail (Tosi, Roatsch, et al., 2024). GALA's ice shell thickness estimates, derived from tidal flexure models, will contextualize RIME's subsurface profiles, revealing whether Antum's shallow depth is anomalous or part of a broader pattern linked to Ganymede's porous crust.

SWI, the Submillimeter Wave Instrument (Hartogh & SWI Team, 2023), will measure surface temperatures on Ganymede to depths of a few millimeters, providing valuable data on thermal inertia and surface composition. By observing in both 600 and 1,200 GHz channels, SWI will offer insights into the vertical variation of thermal properties, helping to distinguish between surface materials such as ice, salts, and other compounds. These measurements will also enable the estimation of the surface's emissivity, which is crucial for understanding properties such as porosity and grain size. Combined with temperature data, SWI will clarify how temperature influences the deposition and retention of volatiles such as water ice and CO_2, and reveal structural characteristics of the surface. Additionally, SWI's data will complement JANUS and MAJIS observations, enhancing our understanding of surface composition and supporting the interpretation of subsurface structures observed by RIME.

The combined use of these instruments will enable a multi-sensor approach to studying the Antum Crater, transforming isolated data sets into a cohesive narrative of impact-driven surface-subsurface exchange. This interdisciplinary approach will not only advance our understanding of Antum Crater but also provide a template for studying other ROI on Ganymede and beyond. Indeed, by integrating data from JANUS, MAJIS, UVS, RIME, GALA, and SWI, JUICE will ultimately reveal the connections between surface features, subsurface processes, and chemical evolution on icy moons, ultimately contributing to the mission's overarching goal of assessing the habitability of Ganymede and other ocean worlds. Through this synergistic exploration, Antum Crater will serve as a microcosm of the dynamic processes that shape icy moons, offering insights into impact mechanics, brine mobilization, and the potential for life beyond Earth.

Conflict of Interest

The authors declare no conflicts of interest relevant to this study.

Data Availability Statement

Galileo SSI and NIMS data sets of Ganymede are archived in NASA's Planetary Data System (PDS) and can be found in Thaller (2000) and Carlson (1998), respectively. The mapping of optical and near infrared spectroscopic data was performed using the commercial software ArcGIS (https://www.arcgis.com/home/index.html). The spectral analysis was performed using homemade software developed in the general-purpose Python

programming language (https://www.python.org). The numerical simulations concerning the Antum impact modeling were carried out using the iSALE shock physics code (https://isale-code.github.io/terms-of-use.html). Data sets for this research are available in Tosi et al. (2025).

Acknowledgments
The authors acknowledge support from the INAF Mainstream project "*Ganimede dal 2D al 3D: Un approccio multidisciplinare in preparazione a JUICE*" (2019–2022), and from the ASI-INAF Grant n. 2023-6-HH.0 (CUP F83C23000070005) "*Missione JUICE—Attività dei team scientifici dei Payload per Lancio, commissioning, operazioni e analisi dati*" (2023–ongoing). We gratefully acknowledge the developers of iSALE-2D, including Gareth Collins, Kai Wünnemann, Dirk Elbeshausen, Tom Davison, Boris Ivanov and Jay Melosh. Some plots in this work were created with the pySALEPlot visualization package written by Tom Davison. We also acknowledge Francesco Marzari for an insightful discussion on the impactor flux in the Jupiter system. This research has made use of the Astrophysics Data System, funded by NASA under Cooperative Agreement 80NSSC21M00561. Open access publishing facilitated by Istituto nazionale di astrofisica, as part of the Wiley - CRUI-CARE agreement.

References

Amsden, A. A., Ruppel, H. M., & Hirt, C. W. (1980). *SALE: A simplified ALE computer program for fluid flow at all speeds (Report No. LA-8095)* (p. 101). Los Alamos National Laboratory Report. LA-8095. https://doi.org/10.2172/5176006

Baby, N. R., Kenkmann, T., Stephan, K., Wagner, R. J., & Hauber, E. (2024). Ray and halo impact craters on Ganymede: Fingerprint for decoding Ganymede's crustal structure. *Earth and Space Science*, *11*(9), e2024EA003541. https://doi.org/10.1029/2024EA003541

Bioucas-Dias, J. M., & Figueiredo, M. A. T. (2010). Alternating direction algorithms for constrained sparse regression: Application to hyperspectral unmixing. *Arxiv, Math, arXiv:1002.4527*. https://doi.org/10.48550/arXiv.1002.4527

Bjonnes, E., Johnson, B. C., Silber, E. A., Singer, K. N., & Evans, A. J. (2022). Ice shell structure of Ganymede and Callisto based on impact crater morphology. *Journal of Geophysical Research: Planets*, *127*(4), e2021JE007028. https://doi.org/10.1029/2021JE007028

Bockelée-Morvan, D., Lellouch, E., Poch, O., Quirico, E., Cazaux, S., de Pater, I., et al. (2024). Composition and thermal properties of Ganymede's surface from JWST/NIRSpec and MIRI observations. *Astronomy and Astrophysics*, *681*, A27. https://doi.org/10.1051/0004-6361/202347326

Bray, V. J., Collins, G. S., Morgan, J. V., & Schenk, P. M. (2008). The effect of target properties on crater morphology: Comparison of central peak craters on the moon and Ganymede. *Meteoritics & Planetary Sciences*, *43*(12), 1979–1992. https://doi.org/10.1111/j.1945-5100.2008.tb00656.x

Bruzzone, L., & Croci, R. (2019). Radar for Icy Moon Exploration (RIME). In *Proceeding of the 2019 IEEE 5th international workshop on metrology for AeroSpace (MetroAeroSpace)*. https://doi.org/10.1109/MetroAeroSpace.2019.8869624

Carlson, R. W. (1998). Galileo NIMS spectral image cubes: Jupiter operations [Dataset]. *NASA Planetary Data System*. https://doi.org/10.17189/1520371

Carlson, R. W., Weissman, P. R., Smythe, W. D., & Mahoney, J. C. (1992). Near-infrared mapping spectrometer experiment on Galileo. *Space Science Reviews*, *60*(1–4), 457–502. https://doi.org/10.1007/BF00216865

Collins, G. C., Patterson, G. W., Head, J. W., Prockter, L., Pappalardo, R. T., Lucchitta, B. K., & Kay, J. P. (2013). Global geologic map of Ganymede. *US Geological Survey*. Scientific Investigations Map 3237. https://doi.org/10.3133/sim3237

Collins, G. S. (2014). Numerical simulations of impact crater formation with dilatancy. *Journal of Geophysical Research: Planets*, *119*(12), 2600–2619. https://doi.org/10.1002/2014JE004708

Collins, G. S., Melosh, H. J., & Ivanov, B. A. (2004). Modeling damage and deformation in impact simulations. *Meteoritics & Planetary Sciences*, *39*(2), 217–231. https://doi.org/10.1111/j.1945-5100.2004.tb00337.x

Croft, S. K., Casacchia, R., & Strom, R. G. (1994). Geologic map of the Tiamat sulcus quadrangle (Jg-9) of Ganymede. *US Geological Survey*. IMAP 2328. https://doi.org/10.3133/i2328

Ding, J. J., Boduch, P., Domaracka, A., Guillous, S., Langlinay, T., Lv, X. Y., et al. (2013). Implantation of multiply charged sulfur ions in water ice. *Icarus*, *226*(1), 860–864. https://doi.org/10.1016/j.icarus.2013.07.002

Filacchione, G., Capaccioni, F., Ciarniello, M., Clark, R. K., Cuzzi, J. N., Nicholson, P. D., et al. (2012). Saturn's icy satellites and rings investigated by Cassini-VIMS: III—Radial compositional variability. *Icarus*, *220*(2), 1064–1096. https://doi.org/10.1016/j.icarus.2012.06.040

Föhn, M., Galli, A., Vorburger, A., Tulej, M., Lasi, D., Riedo, A., et al. (2021). Description of the mass spectrometer for the Jupiter icy moons explorer mission. In *IEEE aerospace conference* (pp. 1–14). https://doi.org/10.1109/AERO50100.2021.9438344

Guest, J. E., Bianchi, R., & Greeley, R. (1988). Geologic map of the Uruk sulcus quadrangle of Ganymede. *US Geological Survey*. IMAP 1934. https://doi.org/10.3133/i1934

Hapke, B. (1984). Bidirectional reflectance spectroscopy 3. Correction for macroscopic roughness. *Icarus*, *59*(1), 41–59. https://doi.org/10.1016/0019-1035(84)90054-X

Hartogh, P., & SWI Team. (2023). The Submillimeter Wave Instrument (SWI) on the JUpiter ICy moons Explorer (JUICE). *55th annual meeting of the division for planetary sciences* (Vol. 55(8), p. 201-02).

Hibbitts, C. A. (2023). Dark ray craters on Ganymede: Impactor or endogenous origin. *Icarus*, *394*, 115400. https://doi.org/10.1016/j.icarus.2022.115400

Hibbitts, C. A., Pappalardo, R. T., Hansen, G. B., & McCord, T. B. (2003). Carbon dioxide on Ganymede. *Journal of Geophysical Research (Planets)*, *108*(E5), 5036. https://doi.org/10.1029/2002JE001956

Hussmann, H., Lingenauber, K., Stark, A., Enya, K., Thomas, N., Lara, L. M., et al. (2025). The Ganymede Laser Altimeter (GALA) on the Jupiter Icy moons Explorer (JUICE) mission. *Space Science Reviews*, *221*(3), 33. https://doi.org/10.1007/s11214-025-01149-7

Ivanov, B. A., Deniem, D., & Neukum, G. (1997). Implementation of dynamic strength models into 2D hydrocodes: Application for atmospheric breakup and impact cratering. *International Journal of Impact Engineering*, *20*(1–5), 411–430. https://doi.org/10.1016/S0734-743X(97)87511-2

Kersten, E., Zubarev, A. E., Roatsch, T., & Matz, K.-D. (2021). Controlled global Ganymede mosaic from voyager and Galileo images. *Planetary and Space Science*, *206*, 105310. https://doi.org/10.1016/j.pss.2021.105310

King, O., & Fletcher, L. N. (2022). Global modeling of Ganymede's surface composition: Near-IR mapping from VLT/SPHERE. *Journal of Geophysical Research: Planets*, *127*(12), e2022JE007323. https://doi.org/10.1029/2022JE007323

Ligier, N., Paranicas, C., Carte, J., Poulet, F., Calvin, W. M., Nordheim, T. A., et al. (2019). Surface composition and properties of Ganymede: Updates from ground-based observations with the near-infrared imaging spectrometer SINFONI/VLT/ESO. *Icarus*, *333*, 496–515. https://doi.org/10.1016/j.icarus.2019.06.013

Liuzzo, L., Poppe, A. R., Paranicas, C., Nénon, Q., Fatemi, S., & Simon, S. (2020). Variability in the energetic electron bombardment of Ganymede. *Journal of Geophysical Research: Space Physics*, *125*(9), e28347. https://doi.org/10.1029/2020JA028347

Luther, R., Raducan, S. D., Burger, C., Wünnemann, K., Jutzi, M., Schäfer, C. M., et al. (2022). Momentum enhancement during kinetic impacts in the low-intermediate-strength regime: Benchmarking and validation of impact shock physics codes. *The Planetary Science Journal*, *3*(10), id.227. https://doi.org/10.3847/PSJ/ac8b89

Mastrapa, R. M., Bernstein, M. P., Sandford, S. A., Roush, T. L., Cruikshank, D. P., & Dalle Ore, C. M. (2008). Optical constants of amorphous and crystalline H2O-ice in the near infrared from 1.1 to 2.6 μm. *Icarus*, *197*(1), 307–320. https://doi.org/10.1016/j.icarus.2008.04.008

McKinnon, W. B., & Schenk, P. M. (1995). Estimates of comet fragment masses from impact crater chains on Callisto and Ganymede. *Geophysical Research Letters*, *22*(13), 1829–1832. https://doi.org/10.1029/95GL01422

Melosh, H. J., Ryan, E. V., & Asphaug, E. (1992). Dynamic fragmentation in impact: Hydrocode simulation of laboratory impacts. *Journal of Geophysical Research*, *97*(E9), 14735–14759. https://doi.org/10.1029/92JE01632

Nesvorný, D., Dones, L., De Prá, M., Womack, M., & Zahnle, K. J. (2023). Impact rates in the outer solar system. *The Planetary Science Journal*, *4*(8), id.139. https://doi.org/10.3847/PSJ/ace8ff

Orton, G. S., Spencer, J. R., Travis, L. D., Martin, T. Z., & Tamppari, L. K. (1996). Galileo photopolarimeter-radiometer observations of Jupiter and the Galilean satellites. *Science*, *274*(5286), 389–391. https://doi.org/10.1126/science.274.5286.389

Palumbo, P., Roatsch, T., Lara, L. M., Castro-Marin, J. M., Della Corte, V., Hviid, S., et al. (2025). The JANUS (Jovis Amorum ac Natorum Undique Scrutator) VIS-NIR multi-band imager for the JUICE mission. *Space Science Reviews*, *221*(3), 32. https://doi.org/10.1007/s11214-025-01158-6

Patterson, G. W., Collins, G. C., Head, J. W., Pappalardo, R. T., Prockter, L. M., Lucchitta, B. K., & Kay, J. P. (2010). Global geological mapping of Ganymede. *Icarus*, *207*(2), 845–867. https://doi.org/10.1016/j.icarus.2009.11.035

Pierazzo, E., Artemieva, N., Asphaug, E., Baldwin, E. C., Cazamias, J., Coker, R., et al. (2008). Validation of numerical codes for impact and explosion cratering: Impacts on strengthless and metal targets. *Meteoritics & Planetary Sciences*, *43*(12), 1917–1938. https://doi.org/10.1111/j.1945-5100.2008.tb00653.x

Poulet, P., Piccioni, G., Langevin, Y., Dumesnil, C., Tommasi, L., Carlier, V., et al. (2024). Moons and Jupiter Imaging Spectrometer (MAJIS) on Jupiter Icy Moons Explorer (JUICE). *Space Science Reviews*, *220*(3), 27. https://doi.org/10.1007/s11214-024-01057-2

Retherford, K. D., Becker, T. M., Gladstone, G. R., Greathouse, T. K., Davis, M. W., Velez, M. A., et al. (2024). Europa ultraviolet Spectrograph (Europa-UVS). *Space Science Reviews*, *220*(8), id.89. https://doi.org/10.1007/s11214-024-01121-x

Schenk, P. M. (2002). Thickness constraints on the icy shells of the Galilean satellites from a comparison of crater shapes. *Nature*, *417*(6887), 419–421. https://doi.org/10.1038/417419a

Scipioni, F., Schenk, P., Tosi, F., D'Aversa, E., Clark, R., Combe, J.-P. H., & Ore, C. D. (2017). Deciphering sub-micron ice particles on Enceladus surface. *Icarus*, *290*, 183–200. https://doi.org/10.1016/j.icarus.2017.02.012

Shkuratov, Y. G., Kreslavsky, M. A., Ovcharenko, A. A., Stankevich, D. G., Zubko, E. S., Pieters, C., & Arnold, G. (1999). Opposition effect from Clementine data and mechanisms of backscatter. *Icarus*, *141*(1), 132–155. https://doi.org/10.1006/icar.1999.6154

Silber, E. A., & Johnson, B. C. (2017). Impact crater morphology and the structure of Europa's ice shell. *Journal of Geophysical Research: Planets*, *122*(12), 2685–2701. https://doi.org/10.1002/2017JE005456

Skinner Jr, J. A., Huff, A. E., Fortezzo, C. M., Gaither, T. A., Hare, T. M., & Hunter, M. A. (2018). Planetary geologic mapping Protocol–2018.

Soderblom, L. A., Barnes, J. W., Brown, R. H., Clark, R. N., Janssen, M. A., McCord, T. B., et al. (2009). Composition of Titan's surface. In R. H. Brown, J.-P. Lebreton, & J. H. Waite (Eds.), *Titan from Cassini-Huygens* (pp. 141–175).

Speagle, J. S. (2020). A conceptual introduction to Markov chain Monte Carlo methods. *Arxiv, stat, arXiv:1909.12313*. https://doi.org/10.48550/arXiv.1909.12313

Stephan, K., Ciarniello, M., Poch, O., Schmitt, B., Haack, D., & Raponi, A. (2021). VIS-NIR/SWIR Spectral properties of H_2O ice depending on particle size and surface temperature. *Minerals*, *11*(12), 1328. https://doi.org/10.3390/min11121328

Stephan, K., Hibbitts, C. A., & Jaumann, R. (2020). H_2O-ice particle size variations across Ganymede's and Callisto's surface. *Icarus*, *337*, 113440. https://doi.org/10.1016/j.icarus.2019.113440

Stephan, K., Hibbitts, C. A., Ligier, N., Molyneux, P., Poulet, F., Prockter, L. M., et al. (2025). Ganymede's surface composition. In M. Volwerk, M. McGrath, X. Jia, & T. Spohn (Eds.), *Ganymede. Planetary science series* (Vol. 28). Cambridge University Press.

Stephan, K., Roatsch, T., Tosi, F., Matz, K.-D., Kersten, E., Wagner, R., et al. (2021). Regions of Interest on Ganymede's and Callisto's surfaces as potential targets for ESA's JUICE mission. *Planetary and Space Science*, *208*, 105324. https://doi.org/10.1016/j.pss.2021.105324

Stickle, A. M., Bruck Syal, M., Cheng, A. F., Collins, G. S., Davison, T. M., Gisler, G., et al. (2020). Benchmarking impact hydrocodes in the strength regime: Implications for modeling deflection by a kinetic impactor. *Icarus*, *338*, 113446. https://doi.org/10.1016/j.icarus.2019.113446

Thaller, T. F. (2000). Galileo orbital operations solid state imaging raw EDR V1.0 [Dataset]. *NASA Planetary Data System*. https://doi.org/10.17189/1520425

Tosi, F., Colaiuta, F., Galluzzi, V., Martellato, E., & Zambon, F. (2025). Data package for the research article: "Antum Crater: A window into Ganymede's icy evolution" [Dataset]. *Zenodo*. https://doi.org/10.5281/zenodo.15482780

Tosi, F., Galluzzi, V., Lucchetti, A., Orosei, R., Filacchione, G., Zambon, F., et al. (2023). Multidisciplinary analysis of the Nippur sulcus region on Ganymede. *Journal of Geophysical Research: Planets*, *128*(7), e2023JE007836. https://doi.org/10.1029/2023JE007836

Tosi, F., Mura, A., Cofano, A., Zambon, F., Glein, C. R., Ciarniello, M., et al. (2024). Salts and organics on Ganymede's surface observed by the JIRAM spectrometer onboard Juno. *Nature Astronomy*, *8*(1), 82–93. https://doi.org/10.1038/s41550-023-02107-5

Tosi, F., Roatsch, T., Galli, A., Hauber, E., Lucchetti, A., Molyneaux, P., et al. (2024). Characterization of the surfaces and near-surface atmospheres of Ganymede, Europa and Callisto by JUICE. *Space Science Reviews*, *220*(5), 59. https://doi.org/10.1007/s11214-024-01089-8

Wünnemann, K., Collins, G. S., & Melosh, H. J. (2006). A strain-based porosity model for use in hydrocode simulations of impacts and implications for transient crater growth in porous targets. *Icarus*, *180*(2), 514–527. https://doi.org/10.1016/j.icarus.2005.10.013

Wünnemann, K., & Ivanov, B. A. (2003). Numerical modelling of the impact crater depth-diameter dependence in an acoustically fluidized target. *Planetary and Space Science*, *51*(13), 831–845. https://doi.org/10.1016/j.pss.2003.08.001

Zahnle, K., Pollack, J. B., Grinspoon, D., & Dones, L. (1992). Impact-generated atmospheres over Titan, Ganymede, and Callisto. *Icarus*, *95*(1), 1–23. https://doi.org/10.1016/0019-1035(92)90187-C

Zahnle, K., Schenk, P., Levison, H., & Dones, L. (2003). Cratering rates in the outer solar system. *Icarus*, *163*(2), 263–289. https://doi.org/10.1016/S0019-1035(03)00048-4

References From the Supporting Information

Belgacem, I., Schmidt, F., & Jonniaux, G. (2021). Regional study of Ganymede's photometry. *Icarus*, *369*, 114631. https://doi.org/10.1016/j.icarus.2021.114631

Berg, B. L., Cloutis, E. A., Beck, P., Vernazza, P., Bishop, J. L., Takir, D., et al. (2016). Reflectance spectroscopy (0.35–8 μm) of ammonium-bearing minerals and qualitative comparison to ceres-like asteroids. *Icarus*, *265*, 218–237. https://doi.org/10.1016/j.icarus.2015.10.028

Bishop, J. L., King, S. J., Lane, M. D., Brown, A. J., Lafuente, B., Hiroi, T., et al. (2021). Spectral properties of anhydrous carbonates and nitrates. *Earth and Space Science*, *8*(10), e01844. https://doi.org/10.1029/2021EA001844

Bray, V. J., Collins, G. S., Morgan, J. V., Melosh, H. J., & Schenk, P. M. (2014). Hydrocode simulation of Ganymede and Europa cratering trends—How thick is Europa's crust? *Icarus*, *231*, 394–406. https://doi.org/10.1016/j.icarus.2013.12.009

Carlson, R. W., Johnson, R. E., & Anderson, M. S. (1999). Sulfuric acid on Europa and the radiolytic sulfur cycle. *Science*, *286*(5437), 97–99. https://doi.org/10.1126/science.286.5437.97

Clark, R. N., & Roush, T. L. (1984). Reflectance spectroscopy: Quantitative analysis techniques for remote sensing applications. *Journal of Geophysical Research*, *89*(B7), 6329–6340. https://doi.org/10.1029/JB089iB07p06329

Cloutis, E., Berg, B., Mann, P., & Applin, D. (2016). Reflectance spectroscopy of low atomic weight and Na-rich minerals: Borates, hydroxides, nitrates, nitrites, and peroxides. *Icarus*, *264*, 20–36. https://doi.org/10.1016/j.icarus.2015.08.026

Collins, G. S., Kenkmann, T., Osinski, G. R., & Wünnemann, K. (2008). Mid-sized complex crater formation in mixed crystalline-sedimentary targets: Insight from modeling and observation. *Meteoritics & Planetary Sciences*, *43*(12), 1955–1977. https://doi.org/10.1111/j.1945-5100.2008.tb00655.x

Collins, G. S., Melosh, H. J., & Osinski, G. R. (2012). The Impact-cratering process. *Elements*, *8*(1), 25–30. https://doi.org/10.2113/gselements.8.1.25

Collins, G. S., Elbeshausen, D., Davison, T. M., Wünnemann, K., Ivanov, B., & Melosh, H. J. (2016). iSALE-Dellen manual. https://figshare.com/articles/journal_contribution/iSALE-Dellen_manual/3473690?file=5472191

Cruz Mermy, G., Schmidt, F., Andrieu, F., Cornet, T., Belgacem, I., & Altobelli, N. (2023). Selection of chemical species for Europa's surface using Galileo/NIMS. *Icarus*, *394*, 115379. https://doi.org/10.1016/j.icarus.2022.115379

Dalton III, J. B., Shirley, J. H., & Kamp, L. W. (2012). Europa's icy bright plains and dark Linea: Exogenic and endogenic contributions to composition and surface properties. *Journal of Geophysical Research*, *117*(E3), E03003. https://doi.org/10.1029/2011JE003909

Davison, T. M., & Collins, G. S. (2022). Complex Crater formation by oblique impacts on the Earth and moon. *Geophysical Research Letters*, *49*(21), e2022GL101117. https://doi.org/10.1029/2022GL101117

De Angelis, S., Carli, C., Tosi, F., Beck, P., Schmitt, B., Piccioni, G., et al. (2017). Temperature-dependent VNIR spectroscopy of hydrated Mg-sulfates. *Icarus*, *281*, 444–458. https://doi.org/10.1016/j.icarus.2016.07.022

De Angelis, S., Tosi, F., Carli, C., Potin, S., Beck, P., Brissaud, B., et al. (2021). Temperature-dependent, VIS-NIR reflectance spectroscopy of sodium sulfates. *Icarus*, *357*, 114165. https://doi.org/10.1016/j.icarus.2020.114165

De Angelis, S., Tosi, F., Carli, C., Beck, P., Brissaud, B., Schmitt, B., et al. (2022). VIS-IR spectroscopy of magnesium chlorides at cryogenic temperatures. *Icarus*, *373*, 11475. https://doi.org/10.1016/j.icarus.2021.114756

Douté, S., Schmitt, B., Lopes-Gautier, R., Carlson, R., Soderblom, L., Shirley, J., et al. (2001). Mapping SO_2 frost on Io by the modeling of NIMS hyperspectral images. *Icarus*, *149*(1), 107–132. https://doi.org/10.1006/icar.2000.6513

Fastelli, M., Comodi, P., Schmitt, B., Beck, P., Poch, O., Sassi, P., & Zucchini, A. (2022). Reflectance spectra (1–5 μm) at low temperatures and different grain sizes of ammonium-bearing minerals relevant for icy bodies. *Icarus*, *382*, 115055. https://doi.org/10.1016/j.icarus.2022.115055

Greeley, R., Pappalardo, R. T., Prockter, L. M., & Hendrix, A. R. (2009). Future exploration of Europa. In R. T. Pappalardo, W. B. McKinnon, & K. K. Khurana (Eds.), *Europa* (pp. 655–696). University of Arizona Press.

Güldemeister, N., Wünnemann, K., & Poelchau, M. H. (2015). Scaling impact crater dimensions in cohesive rock by numerical modeling and laboratory experiments. In G. R. Osinski & D. A. Kring (Eds.), *Large meteorite impacts and planetary evolution V*. Geological Society of America. https://doi.org/10.1130/2015.2518(02

Hapke, B. (1981). Bidirectional reflectance spectroscopy. I—Theory. *Journal of Geophysical Research*, *86*(B4), 3039–3054. https://doi.org/10.1029/JB086iB04p03039

Hapke, B. (2012). Bidirectional reflectance spectroscopy 7. *Icarus*, *221*(2), 1079–1083. https://doi.org/10.1016/j.icarus.2012.10.022

Holsapple, K. A. (1993). The scaling of impact processes in planetary sciences. *Annual Review of Earth and Planetary Sciences*, *21*(1), 333–373. https://doi.org/10.1146/annurev.ea.21.050193.002001

Holsapple, K. A., & Housen, K. R. (2007). A crater and its ejecta: An interpretation of Deep Impact. *Icarus*, *187*(1), 345–356. https://doi.org/10.1016/j.icarus.2006.08.029

Hudson, R. L., Moore, M. H., & Cook, A. M. (2005). IR characterization and radiation chemistry of glycolaldehyde and ethylene glycol ices. *Advances in Space Research*, *36*(2), 184–189. https://doi.org/10.1016/j.asr.2005.01.017

Jones, B. M., Kaiser, R. I., & Strazzulla, G. (2014). UV-Vis, infrared, and mass spectroscopy of electron irradiated frozen oxygen and carbon dioxide mixtures with water. *The Astrophysical Journal*, *781*(2), 85. https://doi.org/10.1088/0004-637X/781/2/85

Kivelson, M. G., Khurana, K. K., & Volwerk, M. (2002). The permanent and inductive magnetic moments of Ganymede. *Icarus*, *157*(2), 507–522. https://doi.org/10.1006/icar.2002.6834

Kokaly, R. F., Clark, R. N., Swayze, G. A., Livo, K. E., Hoefen, T. M., Pearson, N. C., et al. (2017). *USGS spectral library version 7* (Vol. 1035, p. 61). U.S. Geological Survey Data Series. https://doi.org/10.3133/ds1035

Kraus, L. G., Senft, L. E., & Stewart, S. T. (2011). Impacts onto H_2O ice: Scaling laws for melting, vaporization, excavation, and final crater size. *Icarus*, *214*(2), 724–738. https://doi.org/10.1016/j.icarus.2011.05.016

Leroux, K., Guillemin, J.-C., & Krim, L. (2020). Solid-state formation of CO and H_2CO via the CHOCHO + H reaction. *Monthly Notices of the Royal Astronomical Society*, *491*(1), 289–301. https://doi.org/10.1093/mnras/stz3051

Martellato, E., Bramson, A. M., Cremonese, G., Lucchetti, A., Marzari, F., Massironi, M., et al. (2020). Martian ice revealed by modeling of simple terraced crater formation. *Journal of Geophysical Research: Planets*, *125*(10), e06108. https://doi.org/10.1029/2019JE006108

McCord, T. B., Carlson, R. W., Smythe, W. D., Hansen, G. B., Clark, R. N., Hibbitts, C. A., et al. (1997). Organics and other molecules in the surfaces of Callisto and Ganymede. *Science*, *278*(5336), 271–275. https://doi.org/10.1126/science.278.5336.271

McCord, T. B., Hansen, G. B., Fanale, F. P., Carlson, R. W., Matson, D. L., Johnson, T. V., et al. (1998). Salts on Europa's surface detected by Galileo's near infrared mapping spectrometer. *Science*, *280*(5367), 1242–1245. https://doi.org/10.1126/science.280.5367.1242

McCord, T. B., Hansen, G. B., & Hibbitts, C. A. (2001). Hydrated salt minerals on Ganymede's surface: Evidence of an ocean below. *Science*, *292*(5521), 1523–1525. https://doi.org/10.1126/science.1059916

Melosh, H. J. (1979). Acoustic fluidization—A new geologic process. *Journal of Geophysical Research*, *84*(B13), 7513–7520. https://doi.org/10.1029/JB084iB13p07513

Melosh, H. J. (1989). Impact cratering: A geologic process. *Oxford Monographs on Geology and Geophysics*, *11*, 1–245.

MODTRAN extraterrestrial solar irradiance. (n.d.). *MODTRAN extraterrestrial solar irradiance*. National Renewable Energy Laboratory. Retrieved from https://www.nrel.gov/grid/solar-resource/spectra.html

Molyneux, P. M., Greathouse, T. K., Gladstone, G. R., Versteeg, M. H., Hue, V., Kammer, J., et al. (2022). Ganymede's UV reflectance from Juno-UVS data. *Geophysical Research Letters*, *49*(23), e2022GL099532. https://doi.org/10.1029/2022GL099532

Moore, M. H., Ferrante, R. F., Hudson, R. L., & Stone, J. N. (2007). Ammonia water ice laboratory studies relevant to outer Solar System surfaces. *Icarus*, *190*(1), 260–273. https://doi.org/10.1016/j.icarus.2007.02.020

Mura, A., Adriani, A., Sordini, R., Sindoni, G., Plainaki, C., Tosi, F., et al. (2020). Infrared observations of Ganymede from the Jovian InfraRed Auroral mapper on Juno. *Journal of Geophysical Research: Planets*, *125*(12), e06508. https://doi.org/10.1029/2020JE006508

O'Keefe, J. D., & Ahrens, T. J. (1982). Cometary and meteorite swarm impact on planetary surfaces. *Journal of Geophysical Research*, *87*(B8), 6668–6680. https://doi.org/10.1029/JB087iB08p06668

Pappalardo, R. T., Collins, G. C., Head, J. W., Helfenstein, P., McCord, T. B., Moore, J. M., et al. (2004). Geology of Ganymede. In F. Bagenal, T. E. Dowling, & W. B. McKinnon (Eds.), *Cambridge planetary science Jupiter. The planet, satellites and magnetosphere* (Vol. 1, pp. 363–396). Cambridge University Press.

Pappalardo, R. T., Cameron, M. E., Collins, G. E., Head, J. W., Helfenstein, P., Howell, S. M., et al. (2025). Ganymede's Geology. In M. Volwerk, M. McGrath, X. Jia, & T. Spohn (Eds.), *Ganymede. Planetary science series* (Vol. 28). Cambridge University Press.

Pierazzo, E., & Melosh, H. J. (2000). Melt production in oblique impacts. *Icarus*, *145*(1), 252–261. https://doi.org/10.1006/icar.1999.6332

Postberg, F., Sekine, Y., Klenner, F., Glein, C. R., Zou, Z., Abel, B., et al. (2023). Detection of phosphates originating from Enceladus's ocean. *Nature*, *618*(7965), 489–493. https://doi.org/10.1038/s41586-023-05987-9

Quirico, E., & Schmitt, B. (1997). Near-infrared Spectroscopy of simple hydrocarbons and carbon oxides diluted in solid N2 and as pure ices: Implications for Triton and Pluto. *Icarus*, *127*(2), 354–378. https://doi.org/10.1006/icar.1996.5663

Schmitt, B., Quirico, E., Trotta, F., & Grundy, W. M. (1998). Optical properties of ices from UV to infrared. In S. N. Shore (Ed.), *Springer)* solar system ices*, publisher: Dordrecht Kluwer academic publishers* (pp. 199–240). Astrophysics and space science library (ASSL). Series vol no 227. ISBN0792349024.

Schutte, W. A. (1995). The formation of organic molecules in astronomical ices. *Advances in Space Research*, *16*(2), 53–60. https://doi.org/10.1016/0273-1177(95)00193-I

Spohn, T., & Schubert, G. (2003). Oceans in the icy Galilean satellites of Jupiter? *Icarus*, *161*(2), 456–467. https://doi.org/10.1016/S0019-1035(02)00048-9

Thomas, N. H., Ehlmann, B. L., Meslin, P.-Y., Rapin, W., Anderson, D. E., Rivera-Hernández, F., et al. (2019). Mars science laboratory observations of chloride salts in Gale crater, Mars. *Geophysical Research Letters*, *46*(19), 10754–10763. https://doi.org/10.1029/2019GL082764

Tillotson, J. H. (1962). *Metallic equations of state for hypervelocity impact. General Atomic Report, GA-3216*. General Atomic.

Wagner, R., Möhler, O., & Schnaiter, M. (2012). Infrared optical constants of crystalline sodium chloride dihydrate: Application to study the crystallization of aqueous sodium chloride solution droplets at low temperatures. *The Journal of Physical Chemistry A*, *116*(33), 8557–8571. https://doi.org/10.1021/jp306240s

Winter, P. M., Galiazzo, M. A., & Maindl, T. I. (2018). Analysis of close encounters with Ganymede and Callisto using a genetic N-body algorithm. *Frontiers in Astronomy and Space Sciences*, *5*(16), 16. https://doi.org/10.3389/fspas.2018.00016

Erratum

The originally published version of this article omitted the notes from Tables 5 and 6. The following note has been added at the end of Table 5: "The associated uncertainties, derived from the MCMC corner plots, are detailed in Table S3 of Supporting Information S1." The following note has been added at the end of Table 6: "Uncertainties are derived from corner plots and are provided in Table S4 of Supporting Information S1." This may be considered the authoritative version of record.